Coupled Roto-Translational Motion of the Heliogyro Applied to Earth-Mars Cyclers

Heiligers, M.J.; Monechi, Guido

Publication date
2022

Published in
Proceedings of the International Astronautical Congress

Citation (APA)
Heiligers, M. J., & Monechi, G. (2022). Coupled Roto-Translational Motion of the Heliogyro Applied to Earth-Mars Cyclers. In *Proceedings of the International Astronautical Congress*

73rd International Astronautical Congress (IAC), Paris, France, 18-22 September 2022.

IAC–22–C1.9.6

Coupled roto-translational motion of the heliogyro applied to Earth-Mars cyclers

Guido Monechi[a*], **Jeannette Heiligers**[a]

[a] *Faculty of Aerospace Engineering, Delft University of Technology, Kluyverweg 1, Delft, The Netherlands 2629 HS, G.Monechi@student.tudelft.nl, M.J.Heiligers@tudelft.nl*
[*] *Corresponding author*

Solar sailing is a flight-proven low-thrust propulsion technology with strong potential for innovative scientific missions. All previous solar-sail missions employed a solar-sail system design consisting of four triangular sail quadrants supported by deployable booms. As an alternative to such a fixed and flat sail-system design, this paper investigates the dynamics of the heliogyro. The heliogyro is a helicopter-like sail design that utilizes a set of long slender blades which are deployed and flattened by spin-induced tension and whose orientations can be individually controlled. The main advantages of such a design are the easier stowage and deployment, and potentially lower structural mass. Moreover, the individual blade orientation allows higher authority on the forces and moments produced by the sail, but at the same time complicates the heliogyro dynamics. The heliogyro's translational and rotational motions are strongly coupled, with non-trivial relationships between the control inputs and the forces and moments produced by the sail. The purpose of this paper is to investigate for the first time the coupled roto-translational motion of the heliogyro. As tantalizing application, the paper analyzes the heliogyro's performance for Earth-to-Mars stopover cycler trajectories, which could aid the exploration of Mars by providing recurrent propellant-less logistics links between Earth and Mars. Two numerical models to describe the heliogyro coupled roto-translational dynamics are derived; a spin-averaged and a non-averaged model. To design time-optimal heliogyro Earth-to-Mars stopover cycler trajectories, a multiple shooting algorithm is employed and the feasibility of the concept is demonstrated. The resulting trajectories are then compared to those of a traditional fixed-area and flat sail-system design, demonstrating that the heliogyro can perform similar trajectories as the traditional fixed-area and flat sailcraft, without the need of an additional system to control the sailcraft attitude.
Keywords: Heliogyro, Solar sailing, Cycler, Mars, Coupled attitude-orbital motion

Nomenclature

Symbols

A	Total sail area
AR	Aspect ratio
a	Pitch profile amplitude angle
$\mathbf{a}$	Acceleration vector
C	Speed of light
c	Chord length
$\mathbf{c}$	Constraint vector
$\mathbf{F}$	Force vector
$\mathbf{I}$	Identity matrix
J	Mass moment of inertia
$\mathbf{J}$	Mass moment of inertia matrix
k	Constant
L	Luminosity
$\mathbf{M}$	Moment vector
m	Mass
N	Number
$\mathbf{n}$	Sail normal direction
O	Objective
P	Solar pressure
R	Blade span
r	Distance
$\mathbf{r}$	Position vector
$\mathbf{S}$	Sensitivity matrix
$\mathbf{s}$	Solar radiation direction
$\mathbf{u}$	Control vector
$\mathbf{X}$	State vector
α	Cone angle
β	Sail lightness number
β_0	Sail lightness number with zero payload
δ	Clock angle
ϵ	Bus mass ratio
η	Sail efficiency
θ	Second sailcraft attitude angle
ϑ_i	Blade i pitch angle
$\boldsymbol{\kappa}$	Smoothness constant vector
λ	Payload ratio
μ	Standard gravitational parameter
ξ_i	Angle between blade i and blade 1
σ	Solar loading parameter

$\boldsymbol{\Phi}$	State transition matrix
ϕ	First sailcraft attitude angle
φ	Pitch profile phase angle
$\boldsymbol{\chi}$	Vector of design variables
ψ	Third sailcraft attitude angle
ψ_i	Blade i orientation angle
$\boldsymbol{\omega}$	Angular velocity vector

Other notation

$\dot{\square}$	First order time derivative
$\ddot{\square}$	Second order time derivative
$\hat{\square}$	Unit-vector
$\bar{\square}$	Averaged value
$[IJ]$	Rotation from reference frame I to J

Superscripts

k	Denotes phase/ leg
T	Transposed
$[*]$	Expressed in reference frame *

Subscripts

$1, 2, 3$	Denote axis of a reference frame
a	Arrival
b	Blade
bus	Bus
c	Cycler
co	Collective
cy	Cyclic
d	Departure
E	Earth
e	Empty
hp	Half-pitch
M	Mars
t	Transfer
s	Sail system
syn	Synodic
sc	Sailcraft
u	Payload
w	Waiting
$\odot$	Sun

Acronyms

ACS	Attitude Control System
EM	Earth-Mars
ME	Mars-Earth
MMOI	Mass Moment Of Inertia
NLP	Non-Linear Programming
RPM	Rotations Per Minute
SRP	Solar Radiation Pressure
STM	State Transition Matrix

1. Introduction

Solar sailing is a promising propulsion method that exploits the Solar Radiation Pressure (SRP) over a large highly reflective sail membrane to generate thrust [1]. It is a highly attractive option for high-energy missions and space exploration as the thrust is produced without the use of propellants [1]. Solar sailing was first considered as an option in the early 1970s for the design of the Comet Halley Rendezvous Mission, which was later canceled [1]. Since then, solar-sailing technology has significantly progressed and its feasibility has been proven by missions such as IKAROS [2], NanoSail-D2 [3], and LightSail 1 and 2 [4]. Exciting upcoming missions such as NEA Scout [5], Solar Cruiser [6], and ACS3 [7] will continue to increase the technology readiness level and further establish solar sailing as a serious option for any future solar-system exploration mission.

The solar-sail designs of all previously mentioned missions consist of a square-shaped fixed-area sail supported by deployable booms, but other sailcraft designs have been proposed as well. Among the alternative sailcraft designs, the heliogyro stands out as a promising option due to the many potential advantages over square-shaped fixed-area sailcraft. The heliogyro was developed by Richard MacNeal in the late 1960s and was the first sailcraft design proposed for the aforementioned Comet Halley Rendezvous Mission [1, 8, 9].

The heliogyro sailcraft consists of several slender sail blades kept in tension by the sailcraft spin, with a central hub where the bus and payload are located. The orientation of the sail blades (pitch angle) can be modified to control the generated SRP forces and moments, thereby giving the sailcraft a higher control authority compared to traditional fixed-area sailcraft [10, 11]. As moments can be generated and controlled by pitching the sail blades, no separate Attitude Control System (ACS) for the heliogyro is needed, in contrast to fixed-area solar sails that need a system such as sail vanes, sliding masses, or reflectivity control devices to control the sailcraft attitude [12, 13]. As the heliogyro's blades can be stored in spools during launch and deployed through the sailcraft spin, the heliogyro has a significantly easier stowage and deployment process compared to traditional fixed-area solar sails. In addition to that, less supporting structure is required to support the sail thanks to the spin-induced rigidity, potentially allowing for lower mass, larger sailcraft performance, and better scalability compared to traditional fixed-area sailcraft [1].

After the initial developments by MacNeal [8, 9] and subsequent research on the heliogyro by Blomquist [14, 15, 16], limited research was performed

in the following years. Interest in the heliogryo increased again in the 2010s with NASA's HELIOS mission proposal [17], a conceptual low-cost sailcraft to showcase heliogyro technology developments ongoing at NASA [18]. A complete overview of the heliogyro sailcraft design and ongoing research is given in Guerrant's PhD thesis [19]. Current research about the heliogyro is focused on the major uncertainties of the sailcraft concept: the dynamics, structural stability, and control of the flexible sail blades [20, 21, 22, 23]; as well as the modeling of the rotational and translational dynamics of the sailcraft for mission design [10, 24, 25, 26].

In the scarce amount of research on the heliogyro, the rotational and translational dynamics of the sailcraft are usually analyzed independently. Limiting assumptions are often introduced, such as modeling the sailcraft's area as variable and neglecting the sail blades' orientations. These sail blades' orientations directly control *both* the SRP forces and moments generated by the sail, which directly influence both the rotational and translational motion of the sailcraft. Such forces and moments are strongly dependent on the position and orientation of the sailcraft relative to the Sun. The rotational and translational dynamics of the sailcraft are therefore tightly coupled and should be analyzed as such.

The purpose of this paper is to develop two novel models describing the *coupled* roto-translational dynamics of the heliogyro: a spin-averaged model and a non-averaged model. The non-averaged model models the heliogyro rotational motion including the spin-rotation, while the spin-averaged model only models the translational and spin-axis motion, averaging the forces and moments over the heliogyro's spinning rotation. This spin-averaged model is used to design heliogyro stop-over cycler trajectories between Earth and Mars for validation and to showcase its capabilities. A stop-over solar-sail cycler between Earth and Mars can provide a continuous propellant-less logistic connection between the two planets, periodically transporting cargo without the need for refueling. Solar-sail cyclers have been analyzed in the past [27, 28, 29] demonstrating that a solar-sail cycler with a period of two Earth-Mars (EM) synodic periods (approximately 780 Earth days) is possible with mid- to far-term sailcraft performance [28, 29] .

To achieve the aforementioned purpose, this paper is organized as follows. Firstly, in section 2, the heliogyro SRP forces and moments models are described. These models are used for the development of the sailcraft coupled roto-translational dynamics, presented in section 3. Section 4 defines the cycler problem analyzed in this paper, while the trajectory design methodology is presented in section 5. The resulting heliogyro cycler trajectories are presented in section 6 with a comparison to equivalent fixed-area sailcraft cycler trajectories and an analysis of the coupled roto-translational motion of the heliogyro.

2. Heliogyro force & moment models

In this section, the models to compute the heliogyro SRP force and moment vectors are presented. Firstly, in subsection 2.1, a set of reference frames are defined. Later, in subsection 2.2, the "pitch profiles" describing the sail blade orientation are presented, followed by the non-averaged and spin-averaged force and moment models in subsections 2.3 and 2.4, respectively.

2.1 *Reference frames definition*

Several reference frames need to be defined to model the heliogyro dynamics. Note that the reference frames in this work slighly differ from the ones in similar works on the heliogyro [10, 11, 24].

Firstly, two Sun-centered reference frames are defined and visualized in Figure 1. The *Solar* reference frame $S(\hat{\mathbf{s}}, \hat{\mathbf{l}}, \hat{\mathbf{p}})$ is defined with axis $\hat{\mathbf{s}}$ along the Sun-spacecraft vector, $\hat{\mathbf{l}}$ parallel to the ecliptic plane and perpendicular to $\hat{\mathbf{s}}$, and axis $\hat{\mathbf{p}}$ that completes the right-handed reference frame ($\hat{\mathbf{p}} = \hat{\mathbf{s}} \times \hat{\mathbf{l}}$). The *Solar* reference frame is complemented by the *Inertial* reference frame $I(\hat{\mathbf{i}}_1, \hat{\mathbf{i}}_2, \hat{\mathbf{i}}_3)$, which does not rotate during the propagation of the dynamics, with $\hat{\mathbf{i}}_1$ along the same direction as the J2000 epoch mean vernal equinox, $\hat{\mathbf{i}}_3$ normal to the mean ecliptic plane, and $\hat{\mathbf{i}}_2$ completing the frame ($\hat{\mathbf{i}}_2 = \hat{\mathbf{i}}_3 \times \hat{\mathbf{i}}_1$). This frame is used as a base frame for all propagations as it is inertial.

Two other frames are defined, both with the origin in the center of mass of the heliogyro, as shown in Figure 2. First, the *Body* reference frame $B(\hat{\mathbf{b}}_1, \hat{\mathbf{b}}_2, \hat{\mathbf{b}}_3)$ is defined with $\hat{\mathbf{b}}_1$ along blade 1, $\hat{\mathbf{b}}_3$ along the heliogyro spin-axis, and $\hat{\mathbf{b}}_2$ completing the right-handed frame ($\hat{\mathbf{b}}_2 = \hat{\mathbf{b}}_3 \times \hat{\mathbf{b}}_1$). The direction of the $B(\hat{\mathbf{b}}_1, \hat{\mathbf{b}}_2, \hat{\mathbf{b}}_3)$ frame relative to the $I(\hat{\mathbf{i}}_1, \hat{\mathbf{i}}_2, \hat{\mathbf{i}}_3)$ base frame is described through a rotation sequence of three Euler angles (3-2-3) ϕ, θ, and ψ, as shown in Figure 2. Second, the *Despun* reference frame $D(\hat{\mathbf{d}}_1, \hat{\mathbf{d}}_2, \hat{\mathbf{d}}_3)$ is defined. One of the most commonly used approaches for modeling heliogyros is to average force and moments over two rotations, thereby assuming that the spacecraft is rotating uniformly around its spinning axis $\hat{\mathbf{b}}_3$ [11]. When using this assumption it is useful to define the *Despun* reference frame, visualized in Figure 3a, with $\hat{\mathbf{d}}_1$ along blade 1 at the start of a rotation, $\hat{\mathbf{d}}_3$ aligned with the heliogyro spin-axis, and $\hat{\mathbf{d}}_2$ completing the right-handed frame ($\hat{\mathbf{d}}_2 = \hat{\mathbf{d}}_3 \times \hat{\mathbf{d}}_1$).

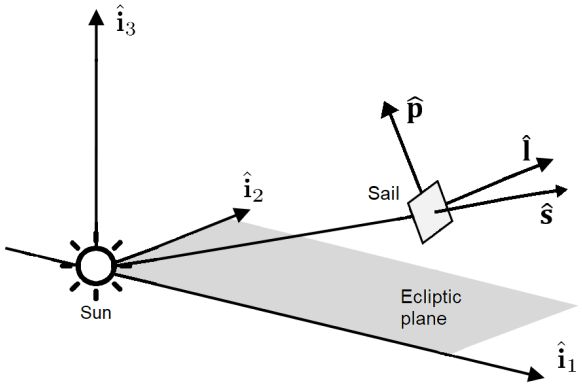

Fig. 1: Relation between the *Solar* and *Inertial* reference frames, adapted from [10].

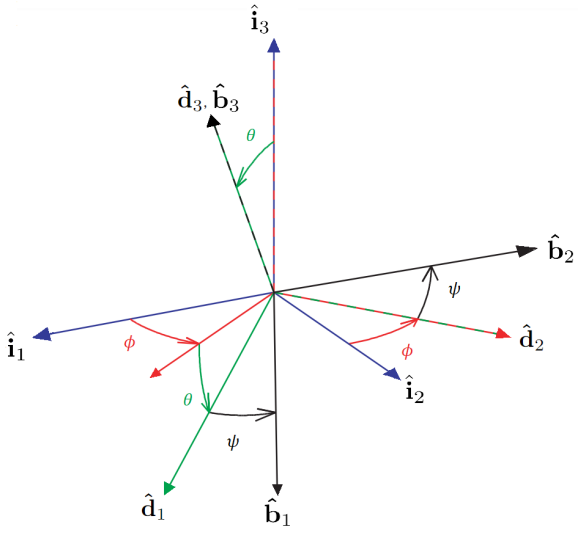

Fig. 2: Relation between the *Body*, *Despun* and *Inertial* reference frames, adapted from [30].

The *Despun* reference frame is one of the intermediate frames in the reference frame transformation from $I(\hat{\mathbf{i}}_1, \hat{\mathbf{i}}_2, \hat{\mathbf{i}}_3)$ to $B(\hat{\mathbf{b}}_1, \hat{\mathbf{b}}_2, \hat{\mathbf{b}}_3)$, as it is the result of the second rotation over the Euler angle θ, as shown in Figures 2 and 3a.

Finally, for each blade i, a local *Blade* reference frame $L_i(\hat{\mathbf{x}}_i, \hat{\mathbf{y}}_i, \hat{\mathbf{z}}_i)$ is defined, as shown in Figure 3b, centered at the central point of the i^{th} blade's root, with axes $\hat{\mathbf{x}}_i$, $\hat{\mathbf{y}}_i$ and $\hat{\mathbf{z}}_i$ along the i^{th} blade span, root chord and normal to blade i respectively.

It is useful to introduce two angles describing the direction of the SRP acceleration vector produced by the sailcraft. These angles are named the "cone" and "clock" angles (α and δ) and are defined relative to the sunlight direction, as shown in Figure 4. The cone angle α is defined as the angle between the sunlight direction $\hat{\mathbf{s}}$ and the SRP acceleration vector, while the clock angle δ is defined as the angle between the axis $\hat{\mathbf{p}}$, perpendicular to the sunlight direction, and the projection of the SRP acceleration vector on the $\hat{\mathbf{p}}$ - $\hat{\mathbf{l}}$ plane [1].

2.2 *Pitch profiles*

Forces and moments acting on the heliogyro can be controlled by varying the pitch angle of each blade. Literature proposes three pitch control laws: collective, cyclic and half-p [8, 11, 14, 19, 25], as visualized in Figure 5. Each profile is explained in the following paragraphs including their use when the spin-axis is aligned with the sunlight direction.

The collective profile pitches all blades at the same constant angle. It is useful to generate a spin-axis moment, for example during blade deployment [19]. The half-p profile pitches the blades sinusoidally over two rotations generating significant torque in the $\hat{\mathbf{d}}_1 - \hat{\mathbf{d}}_2$ plane, which can be useful for slewing (spin-axis precession). In addition to moment, the half-p profile generates a force along the sunlight direction [19]. The cyclic profile pitches the blades sinusoidally over one rotation, generating a force along the sunlight direction and laterally, in the $\hat{\mathbf{d}}_1 - \hat{\mathbf{d}}_2$ plane. No moments are generated [19]. The capacity to generate a lateral force when the sail is perpendicular to the sunlight is unique to the heliogyro as fixed-sailcraft can only generate a force along the sunlight direction in such attitude.

At heliogyro orientations different from Sun-pointing, each pitch profile may generate forces and moments different from what is discussed above. Furthermore, multiple profiles can be used together to combine multiple effects (though note that forces and moments of different profiles do not super-impose [19]). The pitch angle of any blade i can be directly

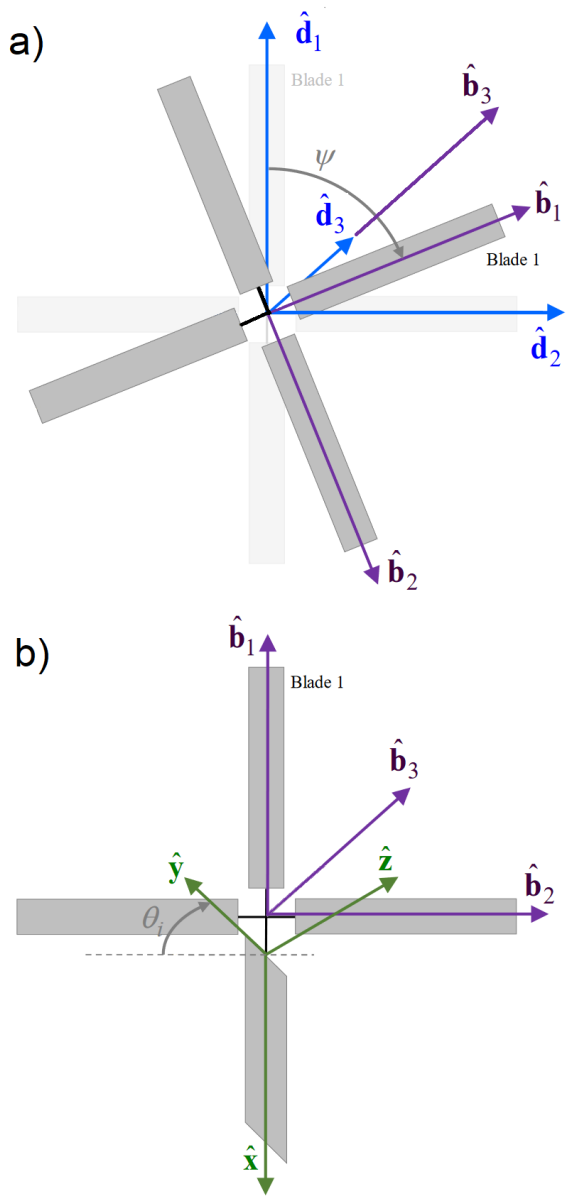

Fig. 3: Visualization of the reference frames *Despun*, *Body*, and *Blade*, adapted from [10]. In a) the relation between the *Despun* and *Body* reference frames is shown. In b) the *Body* and *Blade* reference frames are visualized.

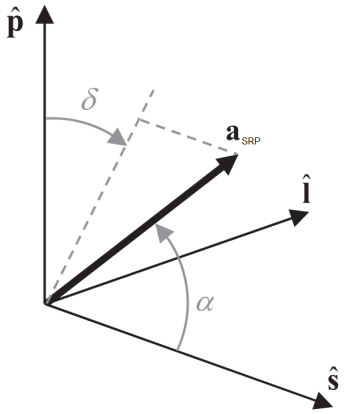

Fig. 4: Visualization of the cone and clock angles of the SRP acceleration vector, $\mathbf{a}_{SRP}$, adapted from [10].

defined using five control variables [24]:

$$\vartheta_i(\psi_i) = -a_{co} + a_{cy}\sin(\psi_i - \varphi_{cy}) + a_{hp}\sin\left[\frac{1}{2}\left(\psi_i - \varphi_{hp} - \frac{\pi}{2}\,\mathrm{sign}(a_{hp})\right)\right] \quad [1]$$

with a_{co}, a_{hp}, and a_{cy} the amplitudes of the collective, half-p, and cyclic profiles, φ_{hp} and φ_{cy} the phase angles of the half-p and cyclic profiles, and ψ_i as:

$$\psi_i = \psi + \xi_i; \qquad \xi_i = 2\pi\frac{i-1}{N_b} \quad [2]$$

with N_b the number of heliogyro blades.

The phase angles φ_{hp} and φ_{cy} can be interpreted geometrically when the spin-axis is aligned with the sunlight direction: with positive half-p amplitude and zero half-p phase angles a lateral moment is produced around the $\hat{\mathbf{d}}_1$ direction. A negative amplitude produces a lateral moment around the $-\hat{\mathbf{d}}_1$ direction. The phase angle rotates the direction of the lateral moment around the $\hat{\mathbf{d}}_3$ axis to span the full $\hat{\mathbf{d}}_1 - \hat{\mathbf{d}}_2$ plane. The same interpretation is valid for the lateral force of the cyclic profile through the phase angle ϕ_{cy}.

2.3 *Non-averaged models*

To derive the SRP force and moment vectors, the following assumptions are made: the solar radiation pressure is assumed to vary with an inverse square law, all sail membranes are assumed to be flat, and photons are assumed to specularly reflect. The SRP forces acting on each blade, expressed in the *Blade* reference frame as shown through the superscript L_i,

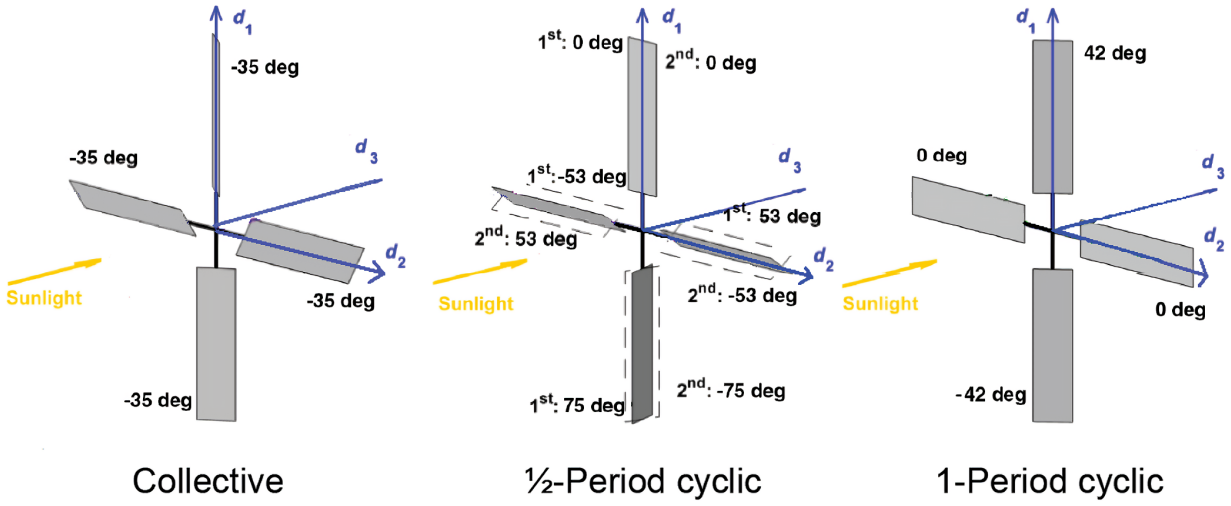

Fig. 5: Heliogyro blade pitch profiles, with dashed lines representing the blade pitch at the second rotation (for half-p), adapted from [10].

can be defined as [1]:

$$\begin{aligned}\mathbf{F}_i^{[L_i]} &= \frac{2P\eta A}{N_b}\left(\hat{\mathbf{s}}^{[L_i]}\cdot\hat{\mathbf{n}}_i^{[L_i]}\right)^2\hat{\mathbf{n}}_i^{[L_i]} \\ &= \frac{L_\odot\eta A}{2\pi C N_b||\mathbf{r}^{[I]}||^2}\left(\hat{\mathbf{s}}^{[L_i]}\cdot\hat{\mathbf{n}}_i^{[L_i]}\right)^2\hat{\mathbf{n}}_i^{[L_i]}\end{aligned} \quad [3]$$

where P is the solar radiation pressure, η is the reflectivity coefficient of the sail material, A is the total area of the heliogyro sail, $L_\odot$ is the solar luminosity constant, C is the speed of light, $\mathbf{r}^{[I]}$ is the heliogyro position relative to the Sun expressed in the *Inertial* reference frame with $||\mathbf{r}^{[I]}||$ as the sailcraft distance from the Sun, $\hat{\mathbf{s}}^{[L_i]}$ is the vector along the incoming solar radiation, and $\hat{\mathbf{n}}^{[L_i]}$ is the normal vector to the blade sail surface (all expressed in the *Blade* reference frame) [10]:

$$\hat{\mathbf{n}}^{[L_i]} = \begin{bmatrix} 0 & 0 & \text{sign}\left(\hat{\mathbf{s}}_3^{[L_i]}\right)\end{bmatrix}^T \quad [4]$$

with $s_3^{[L_i]}$ the third component of the $\hat{\mathbf{s}}^{[L_i]}$ vector. The values used for constants such as C and $L_\odot$ are documented in Table 1.

Table 1: List of constants.

Variable	Value	Unit
$L_\odot$	3.83×10^{26}	W
C	299792458	m/s
$\mu_\odot$	1.327×10^{20}	m^3/s^2
r_E	1	AU
r_M	1.5237	AU

The total instantaneous SRP force acting on the heliogyro, specified in the *Inertial* reference frame, can be computed as:

$$\mathbf{F}^{[I]} = \sum_{i=1}^{N_b}\mathbf{F}_i^{[I]} = \sum_{i=1}^{N_b}[IL_i]\mathbf{F}_i^{[L_i]} \quad [5]$$

with $[IL_i]$ the rotation matrix from the *Blade* reference frame to the *Inertial* reference frame.

To compute the moment generated by the blades the following assumptions are made: the SRP forces are uniformly distributed across the blade surfaces, the center of mass lies on the $\hat{\mathbf{b}}_1-\hat{\mathbf{b}}_2$ plane, and the distance between the blades's root chord and the center of mass is neglected. Under these assumptions, the moments acting on the heliogyro around its center of mass is computed in the *Body* reference frame as:

$$\begin{aligned}\mathbf{M}^{[B]} = \sum_{i=1}^{N_b}\frac{R}{2}\,\hat{\mathbf{x}}_i^{[B]}\times\mathbf{F}_i^{[B]} = \frac{RL_\odot\eta A}{4\pi C N_b||\mathbf{r}^{[I]}||^2} \\ \sum_{i=1}^{N_b}\hat{\mathbf{x}}_i^{[B]}\times\left(\hat{\mathbf{s}}^{[B]}\cdot\hat{\mathbf{n}}_i^{[B]}\right)^2\hat{\mathbf{n}}_i^{[B]}\end{aligned} \quad [6]$$

with R the blade span.

2.4 *Averaged models*

For long-term propagations, it is convenient to compute the average forces and moments over two spin rotations, averaging out high-frequency variations due to the periodic pitch profiles [19].

The averaged SRP force and moment can be computed by integrating the forces and moments acting

on one of the blades (see Eq. 5 and 6) over two spin rotations of the heliogyro, dividing by 4π and multiplying by the number of blades:

$$\bar{\mathbf{F}}^{[I]} = \frac{L_\odot \eta A}{8\pi^2 C ||\mathbf{r}^{[I]}||^2} \int_0^{4\pi} [IB] \left[\left(\hat{\mathbf{s}}^{[B]} \cdot \hat{\mathbf{n}}_1^{[B]} \right)^2 \hat{\mathbf{n}}_1^{[B]} \right] d\psi \quad [7]$$

$$\bar{\mathbf{M}}^{[D]} = \frac{R L_\odot \eta A}{16\pi^2 C ||\mathbf{r}^{[I]}||^2} \int_0^{4\pi} [DB] \left[\hat{\mathbf{x}}_1^{[B]} \times \left(\hat{\mathbf{s}}^{[B]} \cdot \hat{\mathbf{n}}_1^{[B]} \right)^2 \hat{\mathbf{n}}_1^{[B]} \right] d\psi \quad [8]$$

In Equations 7 and 8, blade 1 was used to compute the averaged SRP force and moment, but any other blade would yield the same result. Finally, note that the force and moment vectors are now expressed in the *Inertial* and *Despun* reference frames and the effect of the pitch profile control variables is included in the direction of the blade normal $\hat{\mathbf{n}}_1^{[B]}$.

The definite integrals in Equations 7 and 8 are evaluated numerically using the trapezoidal rule with 50 segments. This number of segments is selected as a suitable compromise between accuracy of the result and required computational effort.

3. Coupled roto-translational dynamics

The rotational and translational motions of the heliogyro are deeply intertwined, as both the forces and moments affecting the dynamics are dependent on the sailcraft attitude, its position relative to the Sun, and the current pitch profile control variables. Consequently, in order to produce feasible heliogyro trajectories, the two motions need to be coupled and modeled simultaneously.

In this section, two novel models to characterize the heliogyro coupled roto-translational dynamics are presented, a non-averaged dynamical model and an spin-averaged dynamical model, similarly to the force and moment models from section 2. Firstly, the general basic rotational and translational models adopted are described in subsection 3.1. Later, in subsection 3.2, the non-averaged coupled roto-translational model is presented, followed by the spin-averaged one in subsection 3.3.

3.1 *Adopted models*

As the focus of this paper is on the *coupling* of the rotational and translational motions and not the fidelity of the resulting trajectories, a simple two-body dynamical model is adopted, similarly to other sailcraft cycler trajectories research [27, 28]. This model only accounts for the gravitational effect of the central body (Sun). Only interplanetary trajectories are analyzed, without any flybys and ignoring the planetary escape and capture phases.

As previously mentioned in subsection 2.1, the sailcraft attitude is described relative to the *Inertial* reference frame through the Euler angles ϕ, θ, and ψ. The heliogyro is assumed to be a rigid body and rotational dynamics are then described through Euler's rotation equations [31]:

$$\mathbf{J}^{[B]} \cdot \dot{\boldsymbol{\omega}}^{[B]} + \boldsymbol{\omega}^{[B]} \times (\mathbf{J}^{[B]} \cdot \boldsymbol{\omega}^{[B]}) = \mathbf{M}^{[B]} \quad [9]$$

where $\mathbf{J}^{[B]}$ is the heliogyro Mass Moment Of Inertia (MMOI) matrix, as later developed in subsection 4.1, $\boldsymbol{\omega}^{[B]}$ the sailcraft angular velocity vector relative to the *Inertial* reference frame, expressed in the *Body* reference frame, and the dot notation representing the first-order derivative relative to time.

The relationship between the Euler angle derivatives and body-fixed angular velocities $\boldsymbol{\omega}^{[B]}$ in the *Body* reference frame is obtained following the methodology presented in [30, 31]:

$$\begin{bmatrix} \dot{\phi} \\ \dot{\theta} \\ \dot{\psi} \end{bmatrix} = \frac{1}{s\theta} \begin{bmatrix} -c\psi & s\psi & 0 \\ s\theta s\psi & s\theta c\psi & 0 \\ c\theta c\psi & -c\theta s\psi & s\theta \end{bmatrix} \boldsymbol{\omega}^{[B]} \quad [10]$$

with s and c representing the sine and cosine functions.

3.2 *Non-averaged model*

The non-averaged model couples the full rotational motion of the heliogyro with the translational one and is described with a set of 12 first-order differential equations. The state $\mathbf{X}$ is defined as:

$$\mathbf{X} = \left[\mathbf{r}^{[I]}, \dot{\mathbf{r}}^{[I]}, \phi, \theta, \psi, \boldsymbol{\omega}^{[B]} \right]^T \quad [11]$$

For brevity, the superscripts describing the reference frames in the which the state variables and MMOI are defined will be omitted from now on.

Two sailcraft performance parameters are defined: the solar loading parameter σ as the ratio between the the sailcraft total mass and its area and the sailcraft lightness number β as the ratio between SRP acceleration and solar gravitational acceleration [1]. The lightness number can be computed as[1]:

$$\beta = \frac{\eta L_\odot A}{2\pi \mu_\odot C m} = \frac{\eta L_\odot}{2\pi \mu_\odot C \sigma} \quad [12]$$

where m is the sailcraft mass and $\mu_\odot$ as the Sun's standard gravitational parameter, see Table 1.

Using the aforementioned simplified two-body model, Eq. 5, and Eq. 12, the time derivative of the heliogyro velocity $\dot{\mathbf{r}}$ is obtained as:

$$\ddot{\mathbf{r}} = -\frac{\mu_\odot}{||\mathbf{r}||^2}\left[1-\frac{\beta}{N_b}\sum_{i=1}^{N_b}[IL_i]\left(\hat{\mathbf{s}}^{[L_i]}\cdot\hat{\mathbf{n}}_i^{[L_i]}\right)^2\hat{\mathbf{n}}_i^{[L_i]}\right] \quad [13]$$

The time-derivative of the Euler angles ϕ, θ, and ψ is computed using Eq. 10, while the time derivative of the body-fixed angular velocities $\boldsymbol{\omega}$ is found by rearranging and combining Eq. 6, Eq. 9, and Eq. 12:

$$\dot{\boldsymbol{\omega}} = \frac{\mu_\odot R\sigma\beta A}{2N_b||\mathbf{r}||^2}\,\mathbf{J}^{-1}\left[\sum_{i=1}^{N_b}\hat{\mathbf{x}}_i^{[B]}\times\left(\hat{\mathbf{s}}^{[B]}\cdot\hat{\mathbf{n}}_i^{[B]}\right)^2\hat{\mathbf{n}}_i^{[B]}-\boldsymbol{\omega}\times(\mathbf{J}\cdot\boldsymbol{\omega})\right] \quad [14]$$

3.3 *Averaged model*

Simulating the non-averaged rotational model of the heliogyro is computationally intensive due to the high-frequency variation of the Euler angle ψ, which represents the heliogyro rotation around its spin-axis. Therefore, an averaged model eliminating the ψ state is also developed, to be used for fast propagations and trajectory optimization, exploiting the spin-averaged force and moment models presented in subsection 2.4.

A set of nine first-order differential equations is used to model the averaged dynamics, with the full state $\bar{\mathbf{X}}$ as:

$$\bar{\mathbf{X}} = [\mathbf{r}, \dot{\mathbf{r}}, \phi, \theta, \omega_3]^T \quad [15]$$

where ω_3 is the third component of the body-fixed angular velocity vector $\boldsymbol{\omega}^{[B]}$.

Analogously to the non-averaged model, the translational dynamics are described using Eq. 13 as:

$$\ddot{\mathbf{r}} = -\frac{\mu_\odot}{||\mathbf{r}||^2}\left[1-\frac{\beta}{4\pi}\int_0^{4\pi}[IB]\left[\left(\hat{\mathbf{s}}^{[B]}\cdot\hat{\mathbf{n}}_1^{[B]}\right)^2\hat{\mathbf{n}}_1^{[B]}\right]d\psi\right] \quad [16]$$

with the double dot notation representing the second-order derivative relative to time.

The averaged rotational motion can be described by rewriting Eq. 9 relative to the *Despun* reference frame, as done in the "Generalized Spinning Model" [32]:

$$\mathbf{J}^{[D]}\cdot\dot{\bar{\boldsymbol{\omega}}}^{[D]} + \bar{\boldsymbol{\omega}}^{[D]}\times(\mathbf{J}^{[D]}\cdot\bar{\boldsymbol{\omega}}^{[D]}) = \bar{\mathbf{M}}^{[D]} \quad [17]$$

with $\mathbf{J}^{[D]}$ the MMOI in the *Despun* reference frame, equal to $\mathbf{J}^{[B]}$ due to the sailcraft's axis-symmetry, $\bar{\boldsymbol{\omega}}^{[D]}$ the angular velocity of the *Body* reference frame relative to the *Inertial* reference frame expressed in the *Despun* frame, and $\bar{\boldsymbol{\omega}}^{[D]}$ the angular velocity vector of the *Despun* frame relative to the *Inertial* frame:

$$\bar{\boldsymbol{\omega}}^{[D]} = \left[\omega_{\hat{\mathbf{d}}_1}, \omega_{\hat{\mathbf{d}}_2}, \omega_3\right];\ \bar{\boldsymbol{\omega}}^{[D]} = \left[\omega_{\hat{\mathbf{d}}_1}, \omega_{\hat{\mathbf{d}}_2}, 0\right] \quad [18]$$

When again omitting the superscripts indicating the frame in which the variables are defined, the time derivative of the angular velocity components in the *Despun* frame can be computed by rewriting Eq. 17 as [32]:

$$\dot{\bar{\boldsymbol{\omega}}} = \begin{bmatrix} -\frac{J_3}{J}\omega_3\omega_{\hat{\mathbf{d}}_2} \\ \frac{J_3}{J}\omega_3\omega_{\hat{\mathbf{d}}_1} \\ 0 \end{bmatrix} + \mathbf{J}^{-1}\bar{\mathbf{M}}^{[D]} \quad [19]$$

with J_3 indicating the MMOI around the heliogyro spin-axis $\hat{\mathbf{d}}_3$, while J represents the MMOI for the remaining (axis-symmetric) axes.

For a spinning sailcraft it is usually reasonable to assume that the change in spin-axis direction is much slower than the spinning and nutation motion, therefore leading to a slower time-variation of $\mathbf{M}^{[D]}$ compared to the aforementioned motions [32]. Using these assumptions, an averaging method can be applied to Eq. 19 to isolate the low-frequency components from the angular velocities [32]:

$$\omega_{\hat{\mathbf{d}}_1} = \frac{-\bar{M}_{\hat{\mathbf{d}}_2}}{J_3\omega_3};\ \omega_{\hat{\mathbf{d}}_2} = \frac{\bar{M}_{\hat{\mathbf{d}}_1}}{J_3\omega_3};\ \dot{\omega_3} = \frac{\bar{M}_{\hat{\mathbf{d}}_3}}{J_3} \quad [20]$$

where $\bar{M}_{\hat{\mathbf{d}}_1}$, $\bar{M}_{\hat{\mathbf{d}}_2}$, and $\bar{M}_{\hat{\mathbf{d}}_3}$ are the three components of $\bar{\mathbf{M}}^{[D]}$.

Finally, adapting Eq. 10 for the body-fixed angular velocity expressed in the *Despun* reference frame ($\tilde{\boldsymbol{\omega}}$, setting ψ to zero), the following first-order averaged rotational equations of motion are found:

$$\begin{bmatrix} \dot{\phi} \\ \dot{\theta} \\ \dot{\omega}_3 \end{bmatrix} = \begin{bmatrix} \frac{\bar{M}_{\hat{\mathbf{d}}_2}}{J_3\omega_3\sin\theta} \\ \frac{\bar{M}_{\hat{\mathbf{d}}_1}}{J_3\omega_3} \\ \frac{\bar{M}_{\hat{\mathbf{d}}_3}}{J_3} \end{bmatrix} \quad [21]$$

4. Problem definition

In this section, the problem to be solved is defined, starting with a description of the heliogyro's design in subsection 4.1. In subsection 4.2, the concepts related to the stop-over cycler are presented. The optimal control problem is defined in subsection 4.3, while all simulation cases are presented in subsection 4.4.

4.1 *Heliogyro design*

The total sailcraft mass m is composed of the sail system mass m_s, the payload mass m_u, and the mass of the bus m_{bus}. The sailcraft empty mass m_e equals the sum of the sail system mass m_s and bus mass m_{bus}. The bus mass ratio ϵ and the payload ratio λ are defined as:

$$\epsilon = \frac{m_{bus}}{m_e} = \frac{m_{bus}}{m_{bus} + m_s} \quad [22]$$

$$\lambda = \frac{m_u}{m} \quad [23]$$

The total sailcraft mass can then be rewritten as:

$$\begin{aligned} m &= m_e + m_u = m_s + m_{bus} + m_u; \\ 1 &= \frac{\sigma_s A}{m} + \frac{m_{bus}}{m_{bus} + m_s}\frac{m - m_u}{m} + \frac{m_u}{m} = \\ &= \frac{\sigma_s A}{m} + \epsilon(1-\lambda) + \lambda; \\ m &= \frac{\sigma_s A}{(1-\epsilon)(1-\lambda)} \end{aligned} \quad [24]$$

where σ_s is the sail system loading parameter defined as the ratio between the sail system mass m_s and the sail area A.

The two sailcraft performance parameters, solar loading σ and sail lightness number β introduced in section 3, can be rewritten as:

$$\sigma = \frac{\sigma_s}{(1-\epsilon)(1-\lambda)} \quad [25]$$

$$\beta = \frac{\eta L_\odot (1-\epsilon)(1-\lambda)}{2\pi C \mu_\odot \sigma_s} = \beta_0(1-\lambda) \quad [26]$$

with β_0 representing the solar lightness number with no payload.

A baseline heliogyro design is presented in Table 2, based on existing mission proposals for heliogyro sailcraft and their expected mid-term sail performance [1, 9, 16, 18, 19]. The blade aspect ratio AR (ratio between blade span R and chord c) is conservatively selected to be 500, half of the maximum aspect ratio for which blades are expected to be still operable in space [16]. These parameters result in a blade span and chord of 912 and 1.8 meters, respectively, and a baseline zero-payload lightness number β_0 of 0.153. Note that the lightness number is larger than the expected lightness number in the mid-term for a fixed-area sailcraft due to the increased performance of the heliogyro design [19], as mentioned earlier in section 1. The baseline case furthermore assumes a payload ratio λ of 0.347, which results in a lightness number β of 0.1. The heliogyro spin rate ω_3 influences the blade structural dynamics and stress experienced at the root of the blade [8]. A baseline value of 0.26 Rotations Per Minute (RPM) is selected based on the spin rate of MacNeal's *Halley's rendezvous heliogyro* design and other historical heliogyro's designs [9, 16]. The spin rate is constrained to remain constant during the propagation of the dynamics due to structural reasons, in order to avoid situations where controlling the flexible blades might become unfeasible.

The MMOI of the fully-deployed heliogyro is dominated by the sail blades due to their length [19], allowing the assumption $R^2 >> c^2$. Neglecting all other minor MMOI contributions apart from the sail blades (payload, bus, sail supporting structure, and so on) and modeling the blades as uniform-mass thin flat plates, the overall MMOI of the sailcraft is approximated as:

$$\begin{aligned} \begin{bmatrix} J_1 \\ J_2 \\ J_3 \end{bmatrix} &\approx m_s \left(\frac{R^2}{3} + \frac{c^2}{12} \right) \begin{bmatrix} \frac{1}{2} \\ \frac{1}{2} \\ 1 \end{bmatrix} \approx \frac{m_s R^2}{3} \begin{bmatrix} \frac{1}{2} \\ \frac{1}{2} \\ 1 \end{bmatrix} \\ &= \frac{A\sigma_s R^2}{3} \begin{bmatrix} \frac{1}{2} \\ \frac{1}{2} \\ 1 \end{bmatrix} = \frac{A^2 \sigma_s AR}{3N_b} \begin{bmatrix} \frac{1}{2} \\ \frac{1}{2} \\ 1 \end{bmatrix} \end{aligned} \quad [27]$$

4.2 *Stop-over cycler definition*

In this paper, heliogyro trajectories for a stop-over EM cycler are designed. Stop-over indicates that the sailcraft's translational states (Cartesian position and velocity) match the planets' states at departure and arrival.

The trajectories of the two planets are approximated as circular and co-planar for simplicity and to allow for cycler periodicity. This approximation is considered valid as the focus of this paper is on the coupling of the sailcraft's translational and rotational motions, so the trajectories are supposed to be only preliminary estimates for mission design. The problem is therefore initially reduced to two-dimensions, with the third components of $\mathbf{r}$ and $\dot{\mathbf{r}}$ constrained to zero, as well as the Euler angle θ limited to $\pm\frac{\pi}{2}$. However, note that the validity of the approach for the 3D case will be demonstrated in subsection 6.3.

The synodic period t_{syn} of Earth and Mars can be computed as:

Table 2: Sailcraft parameters used, based on heliogyro designs from [9, 16, 19]. Parameters that define the design on the left, derived parameters on the right.

Variable	σ_s	A	ϵ	η	λ	N_b	AR	β_0	β	R	c	m	m_e	m_u
Value	7.2	20000	0.2	0.9	0.347	12	500	0.153	0.1	912	1.8	275.6	180	95.6
Unit	g/m^2	m^2	-	-	-	-	-	-	-	m	m	kg	kg	kg

$$t_{syn} = \frac{2\pi}{\sqrt{\frac{\mu_\odot}{r_E^3}} - \sqrt{\frac{\mu_\odot}{r_M^3}}} \quad [28]$$

with r_E and r_M the distance of Earth and Mars from the Sun, respectively equivalent to the orbits semi-major axes due to the circular orbit approximation. Using the values shown in Table 1, the synodic period is computed to be approximately 780 Earth days.

The total cycler period t_c will be the sum of all waiting times and transfer times:

$$t_c = t_t^{EM} + t_w^M + t_t^{ME} + t_w^E \quad [29]$$

where t_w^M and t_w^E are the waiting times at Mars and Earth, while t_t^{EM} and t_t^{ME} are the transfer times of the EM and Mars-Earth (ME) leg, respectively.

The waiting times are computed as:

$$\begin{aligned} t_w^M &= t_d^{ME} - t_a^{EM} + k^M t_{syn} \\ t_w^E &= t_d^{EM} - t_a^{ME} + k^E t_{syn} \end{aligned} \quad [30]$$

where t_a^{EM}, t_d^{EM}, t_a^{ME} and t_d^{ME} are the arrival and departing epochs of the EM and ME cycler legs and k^M and k^E are the smallest non-negative integers that make the waiting times positive. The transfer times of the two cycler legs t_t^{EM} and t_t^{ME} are computed as:

$$\begin{aligned} t_t^{EM} &= t_a^{EM} - t_d^{EM} \\ t_t^{ME} &= t_a^{ME} - t_d^{ME} \end{aligned} \quad [31]$$

The total period of the cycler will be a multiple of the Earth-Mars synodic period, and can be computed by summing all waiting and transfer times. The cycler problem is parameterized by the departure and transfer times of each leg. January 1st, 2024 at midnight (Barycentric Dynamical Time) is used as a reference time.

4.3 *Optimal control problem definition*

The heliogyro cycler problem can be described though an optimal control problem consisting of two legs, the EM leg and the ME leg. In order to limit the required computational effort, the problem dynamics for both legs are modeled through the averaged heliogyro dynamics described in subsection 3.3, reducing the problem to co-planar ($\hat{\mathbf{i}}_1 - \hat{\mathbf{i}}_2$ plane). Note that the assumption of averaged dynamics will be tested against the non-averaged dynamics in subsection 6.3.

The optimal control problem objective O is to minimize the sum of the transfer times t_t^{EM} and t_t^{ME} of the heliogyro cycler (which maximizes the waiting times at the two planets and the number of round-trips between them within a set time-frame):

$$\text{Minimize: } O = t_t^{EM} + t_t^{ME} \quad [32]$$

The reduced state vector $\bar{\mathbf{X}}_r(t)$ is composed of the four co-planar components ($\hat{\mathbf{i}}_1 - \hat{\mathbf{i}}_2$ plane) of the Cartesian position and velocities, the first Euler angle ϕ describing the heliogyro orientation on the $\hat{\mathbf{i}}_1 - \hat{\mathbf{i}}_2$ plane, and the spin rate ω_3. As described earlier, the non-coplanar Cartesian position and velocities components are set to zero, while the second Euler angle is set to to -0.5π. All states are unbounded, except the spin rate which is constrained to the baseline value of 0.26. The reduced control vector $\mathbf{u}_r(t)$ consists of the time-varying pitch profile angles a_{co}, a_{cy}, a_{hp} described in subsection 2.2, and are bounded between $\pm 0.5\pi$. The phase angles are not included for the co-planar case and are set to a constant value of -0.5π to generate forces only in the $\hat{\mathbf{i}}_1 - \hat{\mathbf{i}}_2$ plane and moments in $\hat{\mathbf{d}}_2$ direction. For both legs, the problem can be fully described at any epoch t through the heliogyro state $\bar{\mathbf{X}}_r(t)$ and control vector $\mathbf{u}(t)$.

For each leg, boundary conditions are set such that the heliogyro position and velocity match the ones of the origin and target planets (at the departure and arrival time, respectively).

4.4 *Study cases*

The cases analyzed in this paper are presented in Table 3 and further elaborated in section 6.

Case 1a is the baseline case, using the baseline heliogyro design described in subsection 4.1 and the averaged dynamical model from subsection 3.3 reduced to a 2D co-planar case, as explained earlier in subsection 4.2.

Cases 1b and 1c all use the same baseline heliogyro, but vary the dynamical model. Case 1b simulates part of the EM leg using the non-averaged dynamical model from subsection 3.2, in order to validate the assumptions of the averaged model and to analyze the

Table 3: List of cases simulated. "Dec." indicates "decreasing", "inc." indicates "increasing".

Case ID	**Dynamics**	β^{EM}	β^{ME}	λ^{EM}	λ^{ME}	ω_3 [RPM]
1a	Averaged	0.1	0.1	0.347	0.347	0.26
1b	Non-averaged	0.1	-	0.347	-	0.26
1c	Averaged, 3D	0.1	-	0.347	-	0.26
2	Averaged	Dec. from β_0	Dec. from β_0	Inc. from 0	Inc. from 0	0.26
3	Averaged	Dec. from 0.1	β_0	Inc. from 0.347	0	0.26
4	Averaged	0.1	0.1	0.347	0.347	Inc. from 0.1

heliogyro rotational dynamics. For this case the state used is the non-averaged state from Eq. 11 and the full pitch profiles control variables $a_{co}, a_{hp}, a_{cy}, \varphi_{hp}$, and φ_{cy}. Case 1c simulates the full EM leg using the averaged dynamical model but in 3D, in order to show the validity of the model also in the out-of-plane direction. For the latter case, a non-circular non-co-planar Keplerian approximation of the ephemerides of Earth and Mars is used [33]. The full averaged state from Eq. 15 is used (adding the non-co-planar position component, velocity component, and second Euler angle θ compared to the state from the baseline case 1a), as well as the full pitch profile control vector.

Cases 2, 3 and 4 all use the same state, controls and dynamics as the baseline case 1a, but vary a design parameter of the heliogyro. Case 2 analyzes the sensitivity of the baseline trajectory to the payload ratio (equal for both the EM and ME leg) and therefore the sailcraft performance through the lightness number β. The payload ratio is varied from a value of zero to the maximum value for which the cycler can still be performed within the same amount of EM synodic periods as the baseline case, using uniform steps in the lightness number steps of 0.005.

In case of a resupply mission to a Martian outpost, it might be convenient to maximize the payload ratio for the EM leg, and return to Earth with no payload. This is studied in Case 3, setting the ME payload ratio to zero, and varying the EM payload ratio from the baseline value to the maximum value for which the cycler can still be performed within the same amount of EM synodic periods as the baseline case. Uniform steps in the EM payload ratio of 0.025 are used.

Finally, Case 4 analyzes the sensitivity of the baseline trajectory to the spin rate ω_3. The spin rate is varied from 0.1 RPM to the maximum value for which the cycler can still be performed within the same amount of EM synodic periods as the baseline. Uniform steps in the spin rate of 0.01 RPM are used. Note that these simulations also potentially represent the sensitivity of the trajectory to design parameters that affect the heliogyro's MMOI and generated moments such as N_b, A and AR.

5. Trajectory design

In this section, the methodology used to design the heliogyro cycler trajectories is presented. A multiple shooting algorithm is adopted to transcribe the continuous problem into a Non-Linear Programming (NLP) problem, as described in subsection 5.1. It is preferable to initialize such algorithms with an initial trajectory close to the expected solution to aid convergence, therefore the generation of initial guesses is a critical step. The process of generating such guesses is presented in subsection 5.2.

5.1 *Multiple shooting method*

A multiple shooting algorithm is selected to transcribe the continuous problem into an NLP problem, as it is relatively simple to implement, has high parallelization potential, and has been used for similar solar-sailing and astrodynamics research works [34, 35]. Multiple shooting improves several issues of single-shooting algorithms, including more robustness for highly non-linear problems, with the downside of increasing the dimensionality of the problem [36, 37, 38].

The trajectory of each leg is split into several segments and the state and control vectors at the beginning of each segment are included in the design variables to optimize. Each segment initial state is propagated numerically until the end of the segment and the differences (named defects) between the final propagated states and the initial states of the next segment are enforced to be zero using equality constraints, as shown in Figure 6.

The initial and final propagation times are included in the design variables, such that the complete design variables vector $\boldsymbol{\chi}$ describing both the EM and ME legs is:

$$\begin{aligned}\boldsymbol{\chi} = [&\bar{\mathbf{X}}^{EM}_{r;0}, \bar{\mathbf{X}}^{EM}_{r;1} \dots \bar{\mathbf{X}}^{EM}_{r;N_s}, \mathbf{U}^{EM}_{r}, t^{EM}_{d}, t^{EM}_{t}, \\ &\bar{\mathbf{X}}^{ME}_{r;0}, \bar{\mathbf{X}}^{ME}_{r;1} \dots \bar{\mathbf{X}}^{ME}_{r;N_s}, \mathbf{U}^{ME}_{r}, t^{ME}_{d}, t^{ME}_{t}]\end{aligned} \quad [33]$$

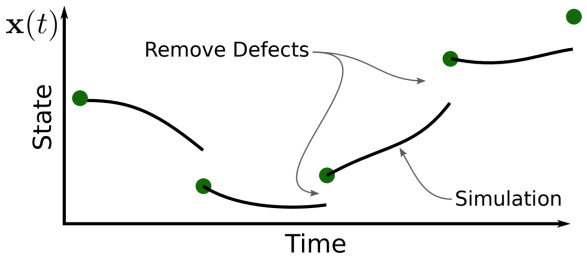

Fig. 6: Visualization of the multiple shooting transcription [38].

with N_s the number of segments, $\bar{\mathbf{X}}^k_{r;j}$ the initial heliogyro state (reduced averaged model, see subsection 4.3) of the j^{th} segment of leg k, and the vector $\mathbf{U}^k_r$ as:

$$\mathbf{U}^k_r = [\mathbf{u}^k_{r;0}, \mathbf{u}^k_{r;1} \dots \mathbf{u}^k_{r;N_s}] \quad [34]$$

with $\mathbf{u}^k_{r;j}$ the reduced control vector (see subsection 4.3) at the initial time of the j^{th} segment of leg k. The control vector is linearly interpolated as a function of time between the $N_s + 1$ grid-points. The subscript notation to indicate the reduced state and controls is omitted from now for simplicity.

For cases 1b and 1c the definition of the design vector is extended from the one in Eq. 33 with the complete control vectors and state vectors as described in subsection 4.4.

The number of segments for the optimization is set to 48, in order to match the number of available parallelization threads in the workstation used, maximizing computational efficiency. Analyses have been performed that highlight that a lower number of segments often result in divergence problems, while a higher number does not improve the quality of the solution (in terms of objective).

The initial conditions of all segments are numerically propagated to the final time using a RK4 integrator, a constant time-step numerical integration method. Variable time-step methods were not considered as they can lead to discontinuities when propagating the State Transition Matrix (STM) [39], therefore leaving constant time-step methods as the most suitable choice. RK4 is chosen because of its popularity and high efficiency compared to other constant time-step numerical integration methods, in terms of numerical accuracy relative to the number of function evaluations [36, 40]. A time-step of 1×10^{-3} synodic periods (i.e. approximately one Earth day) is adopted as it was found to be a good compromise between numerical accuracy and computational effort.

Due to the multiple shooting transcription, the majority of the equality constraints are the defects enforcing a continuous trajectory between segments. For a segment j of leg k, the defect constraint relative to the following segment is defined as:

$$\mathbf{c}^k_j = \tilde{\bar{\mathbf{X}}}^k_{j+1} - \bar{\mathbf{X}}^k_{j+1} \quad [35]$$

where $\tilde{\bar{\mathbf{X}}}^k_{j+1}$ is the state at the beginning of segment $j+1$, propagated from the initial condition of segment j.

The boundary conditions from subsection 4.3 are applied at the initial and final segment as equality constrains. Two inequality constraints are set enforcing that the waiting times at Earth and Mars are higher than 0.01 EM synodic periods (approximately a week). Additional constraints are added to enforce moments $\bar{M}_{\hat{\mathbf{d}}_1}$ and $\bar{M}_{\hat{\mathbf{d}}_3}$ to be equal to zero to keep the spin-rate ω_3 constant and restrict the sailcraft motion to be co-planar with the planets (except for cases 1b and 1c for which the motion is not constrained as co-planar). Other constraints are added to ease the convergence of the optimizer. First, inequality constraints limiting the time derivative of the pitch profiles angles within two degrees per day (absolute value) are introduced, as high angular rates are not expected for long interplanetary trajectories. In addition to that, other constraints are included to avoid sudden jumps on the control vector, by enforcing a constraint in the maximum absolute value of the "concavity" at each grid-point j:

$$|\mathbf{u}^k_{j+1} + \mathbf{u}^k_{j-1} - 2\mathbf{u}^k_j| \leq \boldsymbol{\kappa} \quad [36]$$

with $\boldsymbol{\kappa}$ as an arbitrary vector of constants tuned to achieve the desired results (0.01 radians).

The problem is scaled to avoid numerical errors, as the quantities involved have significantly different orders of magnitude. Positions are normalized in astronomical units, times are scaled by one EM synodic period, and angular velocities are expressed in RPM.

The heliogyro dynamics are implemented in Python. WHORP (version 1.14) is used to solve the discretized optimal control problem as it is particularly suited to solve highly dimensional non-linear problems, often used in space applications [41], it is robust, and has a Python interface through the Pygmo library [42]. As WORHP is a derivative-based solver, the derivatives of the constraints and objective relative to the design vector $\boldsymbol{\chi}$ need to be computed.

Omitting the leg notation for simplicity, the derivatives of the defect constraints relative to the segment j initial state, segment $j+1$ initial state, and the vector $\mathbf{U}$ are:

$$\begin{aligned}\frac{\partial \mathbf{c}_j}{\partial \bar{\mathbf{X}}_j} &= \frac{\partial \tilde{\bar{\mathbf{X}}}_{j+1}}{\partial \bar{\mathbf{X}}_j} = \mathbf{\Phi}(t_{j+1}, t_j) \\ \frac{\partial \mathbf{c}_j}{\partial \bar{\mathbf{X}}_{j+1}} &= -\mathbf{I} \\ \frac{\partial \mathbf{c}_j}{\partial \bar{\mathbf{U}}} &= \frac{\partial \tilde{\bar{\mathbf{X}}}_{j+1}}{\partial \mathbf{U}} = \mathbf{S}(t_{j+1}, t_j)\end{aligned} \quad [37]$$

where $\mathbf{I}$ is the identity matrix, $\mathbf{\Phi}$ is the STM, and $\mathbf{S}$ is the sensitivity matrix (the latter two both from time t_j to time t_{j+1}). Similar derivatives for defects, boundary condition, constraints, and objective, are also computed relative to each component of the design variables vector, but they are not included in this paper for brevity.

During each propagation, the STM and sensitivities matrices are computed through the numerical integration of the variational equations [40]:

$$\begin{aligned}\dot{\mathbf{\Phi}}(t, t_j) &= \frac{\partial \dot{\bar{\mathbf{X}}}(t, \bar{\mathbf{X}}(t))}{\partial \bar{\mathbf{X}}(t)} \mathbf{\Phi}(t, t_j) \\ \dot{\mathbf{S}}(t, t_j) &= \frac{\partial \dot{\bar{\mathbf{X}}}(t, \bar{\mathbf{X}}(t))}{\partial \bar{\mathbf{X}}(t)} \mathbf{S}(t, t_j) + \frac{\partial \dot{\bar{\mathbf{X}}}(t)}{\partial \mathbf{U}}\end{aligned} \quad [38]$$

The derivatives needed to compute the STM, sensitivity matrices, and Jacobian matrices are computed numerically though central finite difference. Sparsity of the Jacobian matrix is exploited to lower the computational effort, computing only the numerical derivative for the non-zero terms. The Hessian matrix is approximated numerically within WORHP [41].

A tolerance of 1×10^{-5} is set on the scaled constraints to achieve easier convergence. Finally, a convergence criterion is set such that the optimizer stops when reaching a scaled optimality of 1×10^{-3} (see the *TolOpti* parameter from the WORHP user manual [43]). All other WORHP settings are set at the default value.

5.2 *Initial guess generation*

The generation of initial guesses is critical for the convergence of the NLP solver when dealing with a highly dimensional non-linear problem. The multi-step process visualized in Figure 7 is adopted, starting with a simple problem and increasing its complexity at each stage, such that for each step the solution of the previous problem can be used as initial guess. This approach is adopted to ease the convergence of the algorithm at each step.

The first step is to find suitable approximate departure dates for both the EM and ME leg, modeling the continuous low-thrust trajectory analytically using logarithmic spirals [1]. The transfer time can be approximated using [1]:

$$\begin{aligned}t_t^{EM} &= \frac{1}{3}\left(r_M^{3/2} - r_E^{3/2}\right)\sqrt{\frac{1-\beta\cos^3\alpha}{\beta^2\mu_\odot\cos^4\alpha\sin^2\alpha}} \\ t_t^{ME} &= \frac{1}{3}\left(r_E^{3/2} - r_M^{3/2}\right)\sqrt{\frac{1-\beta\cos^3\alpha}{\beta^2\mu_\odot\cos^4\alpha\sin^2\alpha}}\end{aligned} \quad [39]$$

with the lightness number β set to 0.1 from the baseline heliogyro design described in subsection 4.1. The cone angle α is optimal at $\pm 35.6°$[1], positive if increasing the orbital semi-major axis and negative if decreasing it. After computing the transfer times, a grid-search is performed varying the departure times for both legs throughout a full EM synodic period to find their values that minimize the miss distance at arrival (from the target planet). The departure time of the ME trajectory is enforced to be after the arrival time of the EM trajectory. The logarithmic spiral trajectories (sailcraft position and velocity) and the departure and transfer times are used as an initial guess for the next step.

The second stage for initial guess generation numerically optimizes the trajectories of a fixed-area solar sail for both the EM and ME legs. The trajectories are combined into the cycler problem, with the waiting time constraints and the objective of minimizing the sum of transfer times, as explained in subsection 4.3. The dynamics used are those in Eq. 13 (therefore omitting the sailcraft rotational dynamics), with the SRP forces from the ideal model in Eq. 3 (setting N_b to 1). WORHP and the multiple shooting transcription are used to solve the optimal control problem, as explained in subsection 5.1, with the sailcraft state and design vector of each leg k as:

$$\begin{aligned}\mathbf{X}_{sc}^k &= [\mathbf{r}, \dot{\mathbf{r}}] \\ \boldsymbol{\chi}_{sc}^k &= \left[\mathbf{X}_{sc;0}^k \dots \mathbf{X}_{sc;N_s}^k, \phi_0 \dots \phi_{N_s}, t_d^{ME}, t_t^{ME}\right]\end{aligned} \quad [40]$$

where the subscript sc indicates that it is the state/design vector for a fixed-area solar sail, other numerical subscripts indicating the segment number, and the Euler angle ϕ used as the only control variable (the problem is reduced to 2D as explained in subsection 4.2). The optimal control solution $\boldsymbol{\chi}_{sc}^k$ fully describes the optimal EM and ME trajectories for a fixed-area solar sail.

The fixed-area solar-sail trajectory can be used as an input for the baseline case described in subsection 4.2 (case 1a). The Euler angle ϕ is converted from a control to a state, because the rotational dynamics are simulated in the baseline case. The pitch profiles control vector $\mathbf{u}_j^k$ is initialized by solving a reduced inverse problem [24], computing the amplitude angles (a_{co}, a_{hp}, and a_{cy}) that generate the required

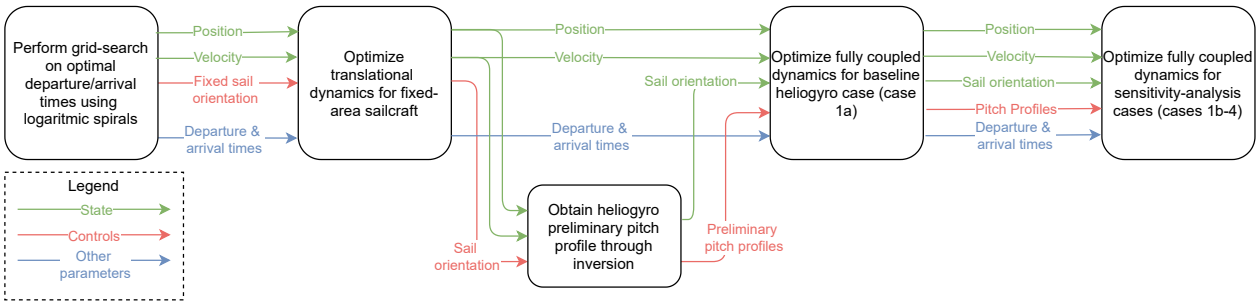

Fig. 7: Visualization of the process to generate initial guesses.

moment and sailcraft acceleration (Equations 7 and 8) to match the initial guess. Firstly, the phase angles (φ_{hp} and φ_{cy}) are set to $-\frac{\pi}{2}$ to generate forces and moments in the required direction. The required time derivative $\dot{\phi}$ is computed numerically (central finite difference) from the initial guess and inserted into Eq. 8 to compute the required moment. The required acceleration is computed from the ideal model in Eq. 3 based on the ideal trajectory ($\mathbf{r}$ and ϕ). Finally, the Nelder-Mead algorithm is used to numerically find the pitch profiles amplitude angles that minimize the acceleration and moments errors, with a convergence criterion of 1×10^{-7} m/s^2 and 1×10^{-7} Nm, respectively. This algorithm is selected as it is simple, available through the SciPy library [44], does not require derivatives (which would have to be numerical for the averaged force and moment models) and works for multi-dimensional problems. In cases of failed convergence for specific time-steps, the converged solution of the nearest time-step is used.

The solution of case 1a is then used as an initial guess for all other cases. For the sensitivity analyses in cases 2 to 4 a continuation method is used such that the solution of the problem with the closest varying input parameter is used as an initial guess.

6. Results & discussion

In this section, the results of the cases defined in subsection 4.4 are presented, following the order described in Figure 7 and subsection 5.2. Cases are named following the nomenclature given in Table 3.

Firstly, the results of the systematic search to analyze the solar-sail cycler feasibility and optimal departure time are presented in subsection 6.1. The results of that analysis are used to generate a fixed-area solar sail cycler solution and the baseline heliogyro cycler solution (case 1a). These results are shown and compared in subsection 6.2. In subsection 6.3, an in-depth analysis of the heliogyro coupled-roto translational motion is performed and presented, analyzing the non-averaged motion results (case 1b) and the non-planar averaged case (case 1c). Finally, in subsection 6.4, sensitivity analyses of the baseline heliogyro cycler are performed for varying lightness numbers, payload ratios of the EM leg, and spin-rates.

6.1 *Cycler departure time systematic search*

As explained in subsection 5.2, an analytical model is used to generate very preliminary interplanetary transfer trajectories. The results of the systematic search are shown in Figure 8, where the departure time of each leg is varied throughout two synodic periods (horizontal axis) and the miss distance at arrival is computed and displayed on the vertical axis. To generate the results, the initial state of the sailcraft from each departure time is forward propagated for 0.55 synodic periods, the transfer times of both the EM and ME legs found from Eq. 39. The miss distances at arrival are computed as the position differences between the sailcraft and the target planet at the arrival times.

The figure shows that for both legs the miss distance is periodic (one synodic period) and has minima around zero, as expected. From the figure, the first optimal opportunity to initiate the EM leg is approximately at $t_d^{EM} = 0.275$, while the optimal departure opportunity for the ME leg is at $t_d^{EM} = 1$. The difference between the departure times of the ME and EM legs is significantly larger than the transfer time of 0.55 synodic periods, therefore allowing the sailcraft to transfer between the two planets in time and indicating that a cycler with a period of two synodic periods is feasible. Note that the transfer times for later results are expected to be longer than this preliminary estimation as the planets' velocities are not matched using the analytical model approximation.

6.2 *Heliogyro/fixed-area solar sail comparison*

The cycler trajectories for the baseline heliogyro cycler (case 1a) and fixed-area solar sail cycler are generated solving the optimal control problems presented in subsection 5.1 and subsection 5.2 , respec-

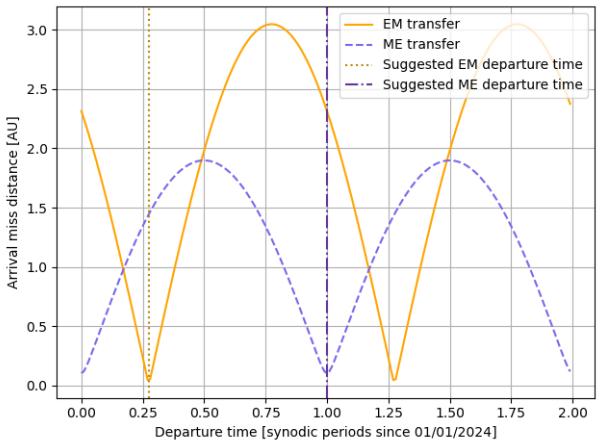

Fig. 8: Arrival miss distance as a function of departure time for both cycler legs.

tively.

The optimal fixed-area solar sail cycler solution is shown in Figure 9. In Figure 9a the two co-planar trajectories for the two legs are shown in the *Inertial* reference frame with arrows showing the magnitude and direction of the SRP acceleration. In Figure 9b the cone angle of the SRP acceleration vector is visualized as a function of time, while the clock angle is not shown as the problem is co-planar (therefore the clock angle is constant).

From the arrows' magnitude and color, it can be seen that the SRP force magnitude is larger when the sailcraft is closer to the Sun, as expected. It can also be observed that the cone angle of the SRP acceleration vector varies around the analytical model optimum of ±35.6 degrees and is axis-symmetric (around the horizontal axis) for the two legs. As expected, the cone angle is positive for the EM leg as the sailcraft needs to increase its velocity, and negative for the ME leg to slow down. Note that for fixed-area solar sails (using an ideal SRP force model) the cone angle of the SRP acceleration vector also describes the sail attitude, as the force is always aligned with the sail normal [1]. This is not necessarily the case for the heliogyro as will be demonstrated later.

Using the fixed-area sailcraft trajectory as an initial guess, the baseline heliogyro cycler solution is computed (case 1a). The transfer and waiting times of the heliogyro and fixed-area solar sail solutions are shown in the first two rows of Table 4, while the resulting heliogyro trajectories for the two legs, as well as the required controls and cone angles of the SRP acceleration vector are shown in Figure 10.

As shown in the table, the total transfer time for the heliogyro is only marginally longer than the fixed-

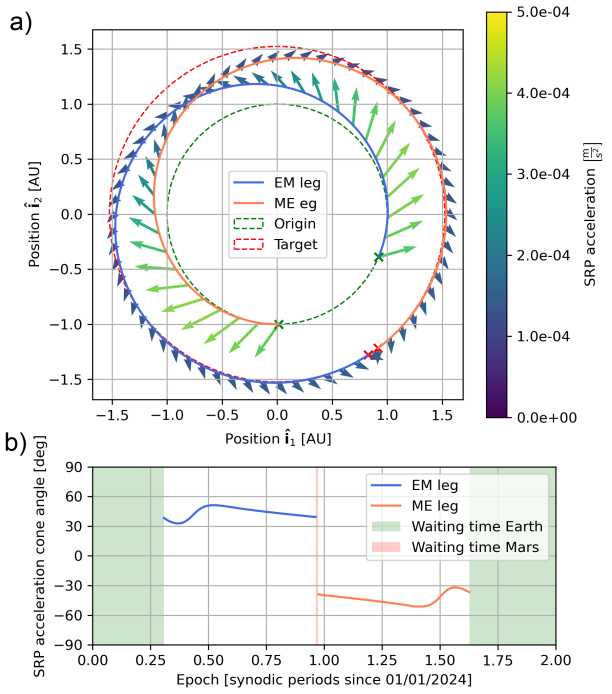

Fig. 9: Fixed-area solar-sail cycler solution. In a) the two legs are presented with arrows to show the force magnitude and direction, while in b) the cone angle of the SRP acceleration vector as a function of time is visualized.

area sailcraft (less than 5%). This is a remarkable finding as the heliogyro is controlling both the sailcraft rotational and translational motion, meaning that no additional ACS is needed. This is not the case for the fixed-area sailcraft as the rotational dynamics aren't taken into account and an additional suitably-sized ACS would be needed, degrading the sailcraft performance. In addition to this, as already mentioned in section 1 and subsection 4.1, fixed-area sailcraft in general would have a smaller zero-payload lightness number compared to heliogyros due to the heavier sail supporting structure, while in this research work they are taken as equivalent.

From Table 4 it is also clear that the waiting time at Mars is equal to 0.01 synodic periods (the minimum allowable value) for both cyclers. From these results, it can be concluded that the waiting time constraint at Mars is active and limiting for both cycler solutions.

The heliogyro cycler trajectory is displayed in Figure 10a together with the SRP acceleration magnitude and direction. It can be seen that the heliogyro cycler legs appear to be similar to the fixed-area solar sail legs. The shorter waiting time at Earth of the

Table 4: Comparison of transfer and waiting times between fixed-area sailcraft cycler, heliogyro baseline cycler (case 1a) and cycler with zero-ME payload (case 2) .

	Transfer time [synodic periods]			**Waiting times [synodic periods]**	
	EM	ME	Total	Earth	Mars
Fixed-area solar sail	0.66	0.65	1.31	0.68	0.01
Baseline heliogyro (case 1a)	0.68	0.68	1.36	0.63	0.01
Zero-ME payload heliogyro (case 2; $\lambda^{EM} = 0.347$; $\lambda^{ME} = 0$)	0.65	0.55	1.20	0.75	0.05

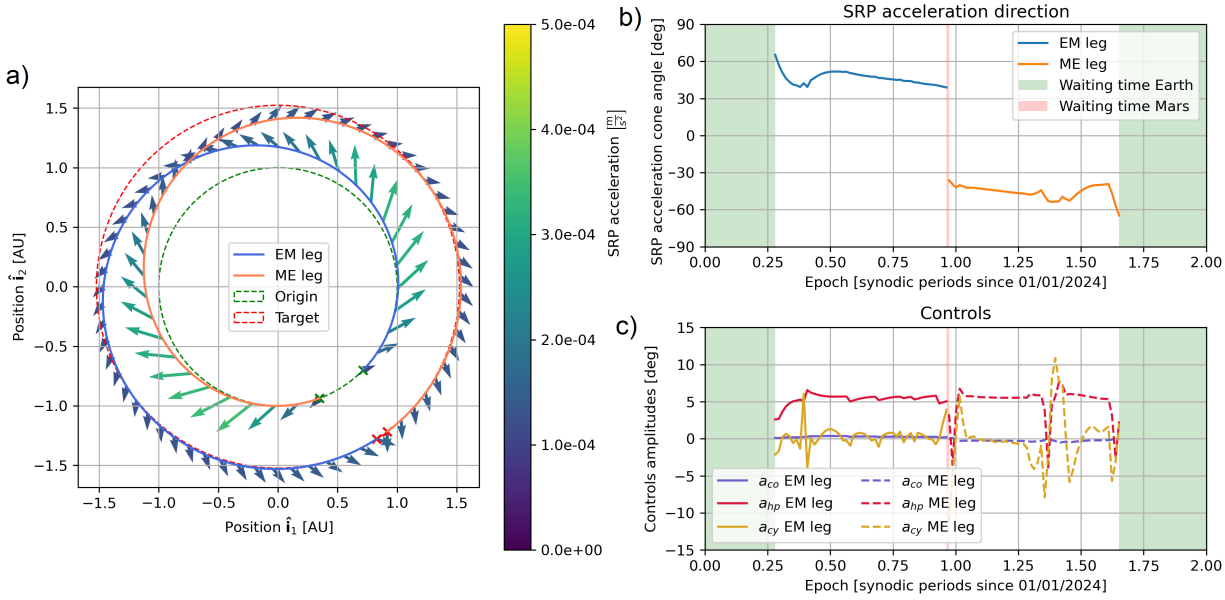

Fig. 10: Case 1a, baseline heliogyro cycler solution. In a) the two leg are presented, with arrows to show the force magnitude and direction, in b) the cone angle of the SRP acceleration vector as a function of time is visualized, while in c) the pitch profile controls $\mathbf{u}_r(t)$ are shown.

heliogyro cycler is also visible when comparing with the fixed-area solar-sail trajectory in Figure 9, as also already highlighted previously in Table 4.

Figure 10b displays the cone angle of the SRP acceleration vector (this time *not* equivalent to the sailcraft orientation) as a function of time. The plot shows that the cone angle is once again varying around the analytical optimal value of ±35.6 degrees and is approximately axis-symmetric around the horizontal axis for the two legs, very similarly to the fixed-area sailcraft shown in Figure 9b. The direction of the heliogyro's spinning axis is not shown in the figure but it differs up to a maximum of 7 degrees from the acceleration direction.

Finally, Figure 10c shows the controls $\mathbf{u}_r(t)$ (pitch profiles angles) as a function of time. A few large and sudden amplitude angle variations are visible and are attributed to the numerical noise of the derivatives used to solve the NLP problem, as previously explained in subsection 5.1. This effect is emphasized by the low sensitivity of the sailcraft state derivatives to the pitch profile angles, as some of the variations of three to five degrees have limited effects on the states derivatives. A relatively constant value (between five and six degrees) of the half-p amplitude (a_{hp}) is visible, while the other two pitch profile amplitudes are varying around zero. The positive half-p amplitude is needed to generate moments around the $\hat{\mathbf{d}}_2$ axis that produce the required rotation rate of the sailcraft ($\dot{\phi}$, see Eq. 21) to keep the heliogyro's spinning axis direction close to the the sunlight direction as the sailcraft revolves around the Sun. On the other hand, the other pitch profile variations are needed to cancel out any moment around $\hat{\mathbf{d}}_3$ (to keep ω_3 constant) and provide the other required force and moment corrections to obtain the optimal trajectory.

Overall, comparing the fixed-area sailcraft cycler with the heliogyro cycler through Table 4, Figure 9, and Figure 10, it can be concluded that the cycler trajectories do not present any major differences. It is shown that the heliogyro performs similarly to the fixed-area solar sail, while not requiring an additional ACS that would degrade sailcraft performance.

6.3 *Heliogyro coupled roto-translational motion*

The coupled roto-translational motion of the heliogyro is analyzed in this subsection by analyzing the heliogyro motion of cases 1b and 1c from Table 3. Both cases use the heliogyro design from the baseline case 1a, but with different dynamical models.

Case 1b uses the non-averaged dynamical model from subsection 3.2 to validate the assumptions of the averaged model for the interplanetary trajectories analyzed within this paper. A one-week section of the EM leg is simulated and the results are visualized in Figure 11. In Figure 11a and b the position and velocity of the heliogyro are shown for the the averaged and the non-averaged models. It can be seen from the two plots that the two dynamical models produce extremely similar trajectories. The final averaged model error is negligible (less than one kilometer in position and one micron per second in velocity). Figure 11c shows the Euler angle ϕ describing the heliogyro orientation as a function of time, once again demonstrating the similarity between the averaged and non-averaged models. As seen in the detail, the non-averaged model produces some high-frequency variations, with the averaged model running through the average of the variations. The high-frequency variations are periodic with a frequency equal to $\frac{\omega_3}{2}$, corresponding to the period of the half-p profile.

In order to show that the trajectory design approach and coupled roto-translational model presented in this paper are also valid for non-co-planar cases, the EM leg is simulated in three-dimensions with case 1c. The resulting EM leg solution is shown in Figure 12. The trajectory itself is shown in Figure 12a, with projections on the three planes of the *Inertial* reference frame $I(\hat{\mathbf{i}}_1, \hat{\mathbf{i}}_2, \hat{\mathbf{i}}_3)$. Note that the motion out of the $\hat{\mathbf{i}}_1$-$\hat{\mathbf{i}}_2$ plane is exaggerated by stretching the $\hat{\mathbf{i}}_3$ axes. The control amplitudes and phases associated with the trajectory are shown in Figure 12b and c. The cone and clock angles of the SRP acceleration vector are displayed as a function of time in Figure 12d, as well as the second Euler angle θ that describes the heliogyro orientation out of the plane $\hat{\mathbf{i}}_1$-$\hat{\mathbf{i}}_2$ plane. The first Euler angle ϕ is not displayed as it simply monotonically increases throughout the trajectory starting from a value around 180 and keeping the angle relative to the Sun around ±35.6 degrees, similarly to case 1a.

As shown in Figure 12d, the second Euler angle θ is always approximately -90 degrees which indicates that the $\hat{\mathbf{d}}_1$ axis is always approximately aligned with the $\hat{\mathbf{i}}_3$ axis. The collective profile amplitude is close to zero throughout the trajectory, in order to generate zero moment $\bar{\mathbf{M}}_{\hat{\mathbf{d}}_3}$ (see Eq. 21). The half-p profile amplitude is a relatively constant positive angle in order to keep the heliogyro spin-axis close to the sunlight direction as the sailcraft revolves around the Sun.

As a reminder for the reader, a positive half-p amplitude with a zero phase angle produces a moment around the $\hat{\mathbf{d}}_1$ axis (the exact effect depends on the sailcraft orientation). The half-p phase angle rotates this moment around the $\hat{\mathbf{d}}_3$ to span the full $\hat{\mathbf{d}}_1$-$\hat{\mathbf{d}}_2$ plane. The same is valid for the cyclic profile, which generates a lateral force component towards the $\hat{\mathbf{d}}_1$

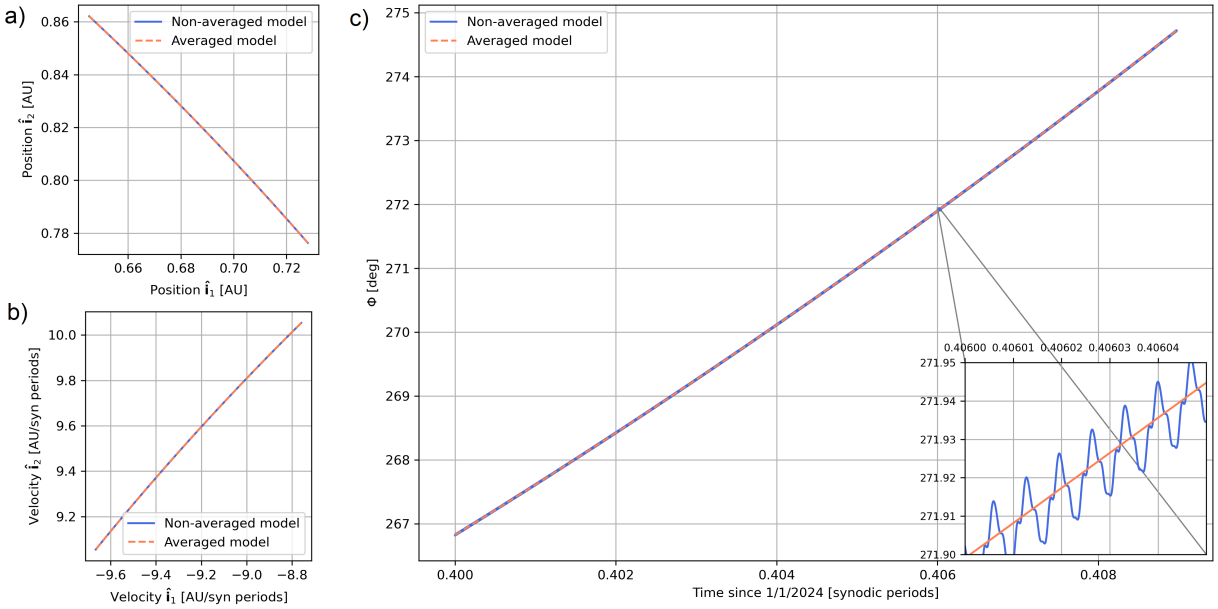

Fig. 11: Case 1a/1b, non-averaged model/averaged model comparison. Figures a) and b) display the position and velocity of the heliogyro, respectively, while c) shows the Euler angle ϕ describing the heliogyro orientation.

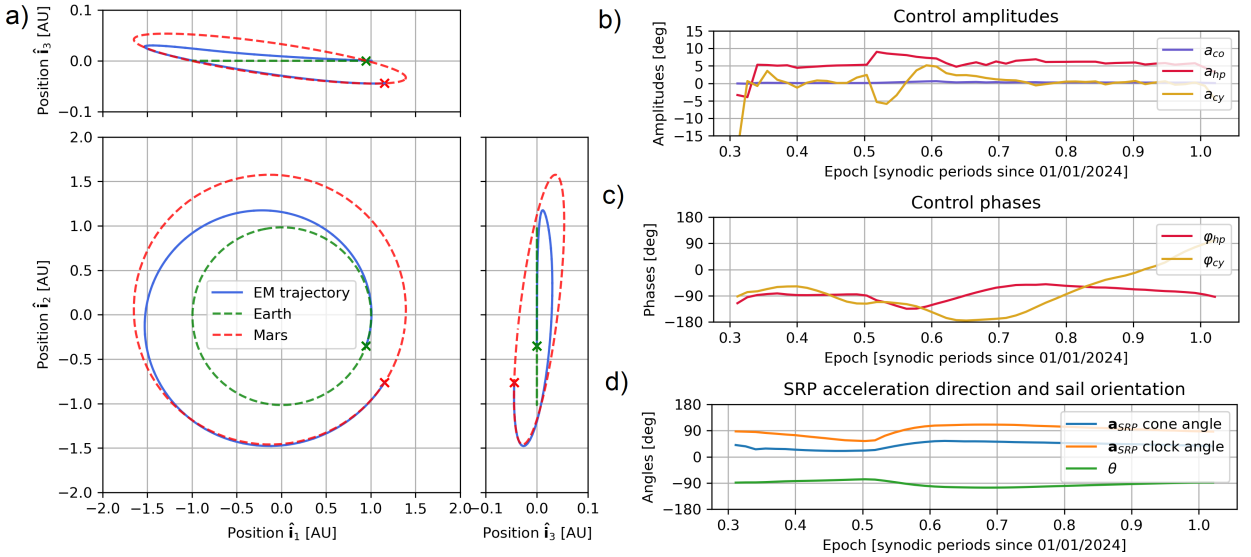

Fig. 12: Case 1c, non-co-planar EM trajectory. Figure a) shows the heliogyro trajectory on three perpendicular planes. Note that the $\hat{\mathbf{i}}_3$ axes are stretched to show the heliogyro motion out of the $\hat{\mathbf{i}}_1$-$\hat{\mathbf{i}}_2$ plane. The pitch profile controls $\mathbf{u}$ are shown in b) and c) (amplitude and phases, respectively). Cone and clock angles of the SRP acceleration vector, as well as the second Euler angle θ describing the heliogyro orientation out-of-plane are displayed in d).

axis with a positive amplitude and zero phase angle (in addition to a component in the $\hat{\mathbf{d}}_3$ direction, with the exact effect dependent on the sailcraft orientation). The lateral force component rotates around the $\hat{\mathbf{d}}_3$ axis as a function of the cyclic phase angle (positive phase angle produces a positive rotation) to span the full $\hat{\mathbf{d}}_1$-$\hat{\mathbf{d}}_2$ plane.

Analyzing Figure 12c, the half-p phase angle varies around -90 degrees, to obtain a moment around $-\hat{\mathbf{d}}_2$ which produces a positive $\dot{\phi}$, see Eq. 21, considering that the Euler angle θ is approximately -90 degrees. Variations above -90 degrees also generate a moment component around the positive $\hat{\mathbf{d}}_1$ direction, therefore producing a positive $\dot{\theta}$, as explained in Eq. 21 and seen in Figure 12d. Similarly, half-p phase angles below -90 degrees produce negative $\dot{\theta}$. This movement out-of-plane is required to match Mars' orbital inclination.

The cone angle of the SRP acceleration vector has a similar profile as the one from case 1a explained earlier in subsection 6.2. The clock angle of the SRP acceleration vector varies around 90 degrees, meaning that the forces are mostly directed towards the $\hat{\mathbf{l}}$ axis, as expected, to increase the sailcraft tangential velocity. Initially, the clock angle is slightly below 90 degrees, meaning the force vector is also pointing slightly towards the $\hat{\mathbf{p}}$ axis, which also corresponds approximately to the $\hat{\mathbf{d}}_1$ direction and the $\hat{\mathbf{i}}_3$ direction, as mentioned previously. This upward movement is needed to match Mars' orbital inclination. Later, the clock angle goes above 90 degrees, which allows the sailcraft to move towards $-\hat{\mathbf{i}}_3$ to reach Mars.

The generation of these out-of-plane ($\hat{\mathbf{i}}_1$-$\hat{\mathbf{i}}_2$ plane) forces that are visible in the clock angle profile from Figure 12d can be explained by looking at the combination of amplitude and phase angles of the cyclic profile (a_{cy} and φ_{cy}): when the amplitude is positive and the phase is above -90 degrees, a force component towards $+\hat{\mathbf{d}}_1$ is generated (corresponding to a clock angle less than 90 degrees). A force component towards $+\hat{\mathbf{d}}_1$ is also generated when the amplitude is negative, and the phase angle is below -90 degrees. Instead, when the amplitude angle is positive and the phase angle is below -90 degrees, a force component towards $-\hat{\mathbf{d}}_1$ is generated (corresponding to a clock angle larger than 90 degrees).

Overall, the heliogyro is capable of completing the three-dimensional EM leg in 0.71 synodic periods, which constitutes an increase of less than 5% compared to the co-planar trajectory transfer time. Through the two cases, it is shown that the averaged model is suitable for modeling the coupled roto-translational motion of the heliogyro for co-planar interplanetary trajectories. In addition to that, it is demonstrated that the trajectory design approach is capable of solving the heliogyro interplanetary transfer problem also in the non-co-planar cases to generate more realistic trajectories.

6.4 *Heliogyro trajectory sensitivity analysis*

This sub-section presents the sensitivity of the baseline cycler (case 1a) by independently varying the payload ratio of both legs (same for both legs, case 2), the payload ratio of only the EM leg (with payload ratio of the ME leg set to zero, case 3), and the spin-rate (case 4), as described in subsection 4.4 and Table 3.

The results of the sensitivity analysis relative to the payload ratio of both legs (and therefore lightness number, case 2) are visualized in Figure 13. The resulting cycler trajectories as a function of lightness number are shown in Figure 13a. Different colors indicate different lightness numbers/payload ratios. The transfer and waiting times of the resulting trajectories are shown in Figure 13b. It can be seen how the transfer times decrease for larger sailcraft performance, i.e. smaller payload ratio or larger lightness number, while the waiting times increase, as expected. For all cases, the sum of all waiting and transfer times equals two synodic periods, the cycler period. The waiting time at Mars is the limiting constraint which makes the two-synodic periods cycler unfeasible for lightness numbers less than 0.098 ($\lambda = 0.36$). Furthermore, even at maximum lightness number, β_0, the sum of the transfer times is above one synodic period, therefore indicating that a much larger sailcraft performance is needed for a one-synodic period cycler. Even if the sum of the transfer times would be slightly below one synodic period, the cycler still would not have a period of one synodic period due to the non-optimal relative position between Earth and Mars, which would force the sailcraft to have non-negligible waiting times.

The cycler trajectory when only transporting payload on the EM leg (case 3) is shown in Figure 14. Two trajectories are shown to highlight the differences: in orange the baseline cycler (case 1a, $\lambda^{EM} = 0.347$; $\lambda^{ME} = 0.347$) and in blue the case transporting payload only on the EM leg ($\lambda^{EM} = 0.347$; $\lambda^{ME} = 0$). The waiting and transfer times of the aforementioned cases are also shown in the second and third row of Table 4.

From the table it becomes clear that both transfer times of the zero-ME-payload are shorter. The difference between the two trajectories is also clearly visible in the figure. The EM leg of the zero-ME-payload cycler has a shorter transfer time and departs slightly later to arrive with more optimal conditions at Mars (as there are looser constraints on the returning ME

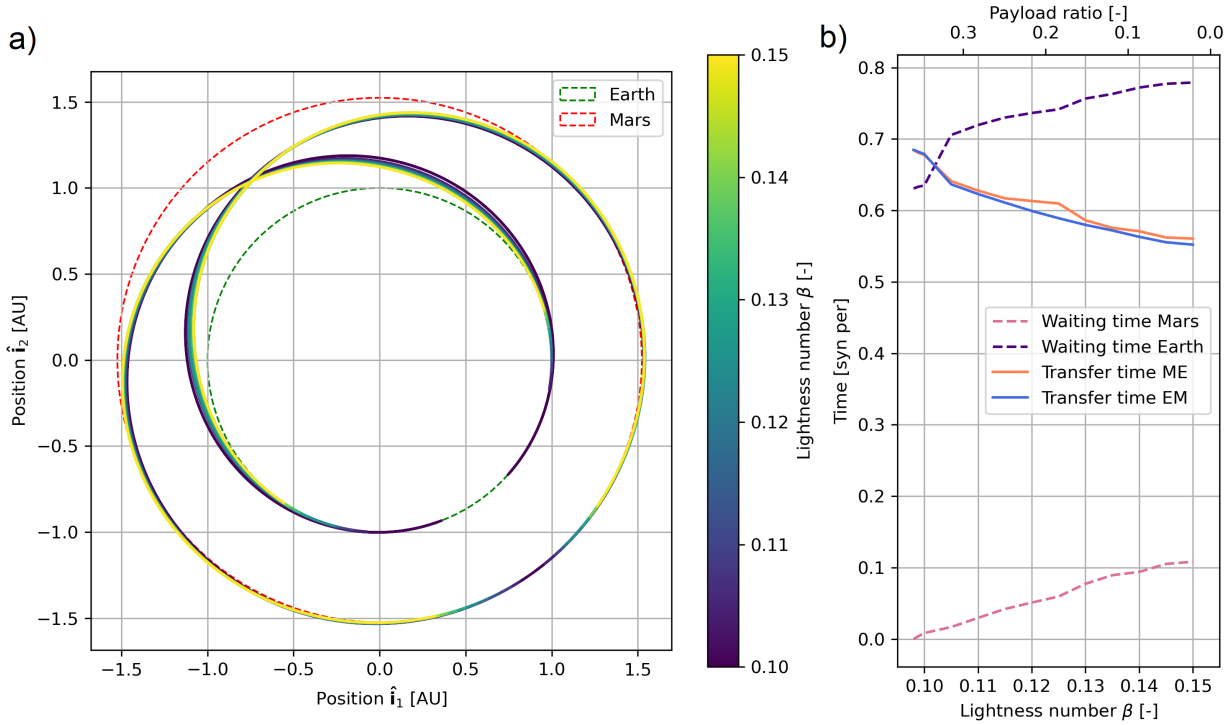

Fig. 13: Case 2, sensitivity analysis relative to the payload ratio of both legs/lightness number. In a) the cycler trajectories are shown with different colors for each lightness number. In b) the transfer and waiting times are plotted as a function of lightness number.

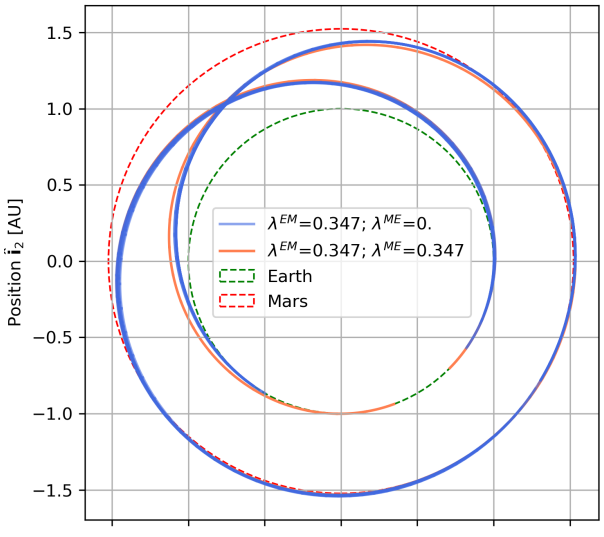

Fig. 14: Cycler trajectory comparison between baseline case (case 1a) and cycler with $\lambda^{EM} = 0.347$ and $\lambda^{ME} = 0$ (case 3).

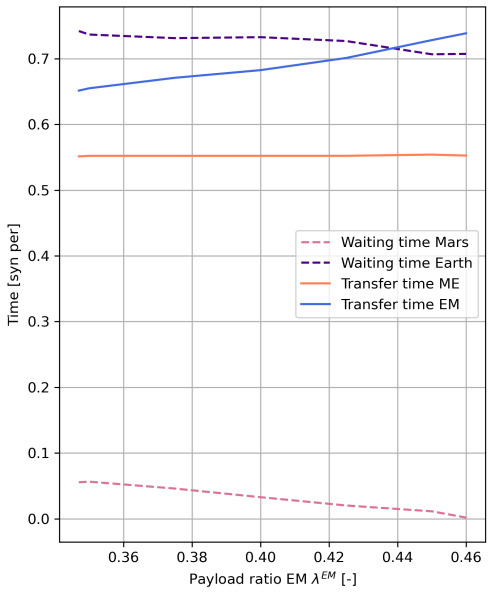

Fig. 15: Case 3, cycler transfer and waiting times as a function of EM payload ratio; with zero ME payload ratio.

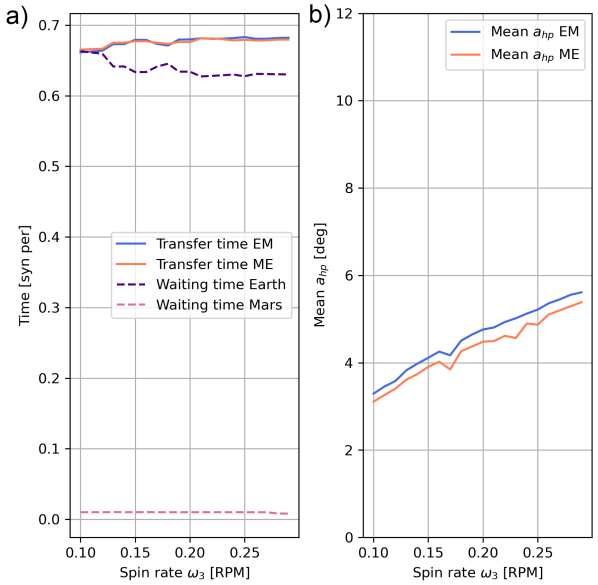

Fig. 16: Case 4, cycler sensitivity as a function of spin-rate ω_3. In a) the waiting and transfer times are shown as a function of spin-rate, while in b) the mean amplitude of the half-p pitch profile is plotted as a function of the spin-rate for the two legs separately.

leg because of the shorter transfer time). After waiting at Mars, the ME leg arrives back at Earth significantly earlier than the baseline cycler, due to the shorter transfer time thanks to the better sailcraft performance with zero-payload.

The waiting and transfer times of the cycler trajectories are displayed as a function of EM payload in Figure 15. Note that the ME payload ratio λ^{ME} is set to zero. Transfer times of the ME legs are constant, while the transfer time of the EM leg increases with increasing EM payload ratio. This is expected as the sailcraft performance is the same for all ME legs while it decreases for the EM legs with larger EM payload ratio. Waiting times also decreases with increasing EM payload ratio, up to the highest feasible EM payload ratio of 0.46 which makes the waiting time at Mars approach zero. By increasing the payload ratio by approximately 11% (from 0.347 to the maximum of 0.46), 60% more payload mass can be transported, making this option very attractive in case no payload from Mars to Earth needs to be transported.

Finally, the results of the sensitivity analysis of the cycler trajectory with respect to the spin-rate ω_3 are displayed in Figure 16. In Figure 16a the transfer and waiting times are shown as a function of the spin-rate. The transfer time increases with increasing spin-rate, but the trend is not as clear as the other sensitivity analyses presented earlier. The mean amplitude of the half-p profile for each leg is shown as a function of spin-rate in Figure 16b. This is shown because the required moment to achieve the same sailcraft rotation rate $\dot{\phi}$ varies as a function of spin-rate ω_3 (see Eq. 21) and the generated SRP moment magnitude is a function of the amplitude of the half-p profile a_{hp}. As expected, there is a direct proportionality between the mean amplitude of the half-p profile and the sailcraft spin-rate. For a larger spin-rate, a larger moment is needed to generate the same sailcraft rotation rate $\dot{\phi}$ (gyroscopic stiffness, see Eq. 21). This larger moment is generated by increasing the amplitude of the half-p profile. The maximum spin-rate that still allows for a non-zero waiting time at Mars is 0.29 RPM.

Overall, the sensitivity analyses in this section demonstrate that the heliogyro has significant flexibility in terms of enabling a two-synodic period cycler even when varying many of the most critical design parameters.

7. Conclusion

Two novel models describing the heliogyro coupled roto-translational dynamics have been presented in this paper. The spin-averaged model was used to design Earth-to-Mars cycler trajectories with a cycler period of two Earth-Mars synodic periods (approximately 780 Earth days).

The heliogyro coupled roto-translational motion was showcased and analyzed both in two and three dimensions, demonstrating that the spin-averaged model can be used for trajectory design as a part of initial mission design. The results of the non-averaged model were compared to the spin-averaged model demonstrating the validity of the assumptions underlying the spin-averaged model in the context of interplanetary trajectories.

The heliogyro trajectories were compared to fixed-area sailcraft cycler trajectories with equivalent sailcraft-performance. It was shown that the heliogyro achieves similar transfer times as the fixed-area sailcraft trajectories, without the need of an additional attitude control system that may degrade the sailcraft performances. Finally, several sensitivity analyses were performed to demonstrate the flexibility and robustness of the heliogyro design which demonstrated that a two-synodic-period cycler is feasible even when varying critical design parameters of the heliogyro.

References

[1] C. McInnes. *Solar Sailing: Technology, Dynamics and Mission Applications*. Springer Praxis Books. Springer Berlin Heidelberg, 2010.

[2] Y. Tsuda, O. Mori, R. Funase, et al. Achievement of IKAROS — Japanese deep space solar sail demonstration mission. *Acta Astronautica*, 82(2):183–188, 2013.

[3] D. Alhorn, J. Casas, E. Agasid, et al. NanoSail-D: The Small Satellite That Could!, 2011.

[4] D. A. Spencer, B. Betts, J. M. Bellardo, et al. The LightSail 2 solar sailing technology demonstration. *Advances in Space Research*, 67(9): 2878–2889, 2021.

[5] T. R. Lockett, J. Castillo-Rogez, L. Johnson, et al. Near-Earth Asteroid Scout Flight Mission. *IEEE Aerospace and Electronic Systems Magazine*, 35(3):20–29, 2020.

[6] J. B. Pezent, R. Sood, A. Heaton, et al. Preliminary trajectory design for NASA's Solar Cruiser: A technology demonstration mission. *Acta Astronautica*, 183:134–140, 2021.

[7] W. K. Wilkie. Overview of the NASA Advanced Composite Solar Sail System (ACS3) Technology Demonstration Project. In *AIAA Scitech 2021 Forum*, 2021.

[8] R. MacNeal. The Heliogyro - An Interplanetary Flying Machine. Technical report, Astro Research Corporation, 1967.

[9] Macneal-Schwendler corporation. Heliogyro preliminary design, phase II Final Report. Technical report, Jet Propulsion Laboratory, 1978.

[10] J. Heiligers, D. Guerrant, and D. Lawrence. Exploring the Heliogyro's Orbital Control Capabilities for Solar Sail Halo Orbits. *Journal of Guidance, Control, and Dynamics*, 40(10):2569–2586, 2017. Publisher: American Institute of Aeronautics and Astronautics.

[11] D. Guerrant and D. Lawrence. Heliogyro Attitude Control Moment Authority via Blade Pitch Maneuvers. In M. Macdonald, editor, *Advances in Solar Sailing*, pages 667–686. Springer Berlin Heidelberg, Berlin, Heidelberg, 2014.

[12] B. Wie. Solar Sail Attitude Control and Dynamics, Part 1. *Journal of Guidance, Control, and Dynamics*, 27(4):526–535, 2004.

[13] B. Wie. Solar Sail Attitude Control and Dynamics, Part Two. *Journal of Guidance, Control, and Dynamics*, 27(4):536–544, 2004.

[14] R. S. Blomquist. *Design study of a solid-state heliogyro solar sail*. PhD thesis, MIT, 1990.

[15] R. Blomquist. Solar blade nanosatellite development: Heliogyro deployment, dynamics, and control. In *AIAA/USU Conference on Small Satellites*, 1999.

[16] R. S. Blomquist. *Heliogyro Control*. PhD thesis, Carnegie Mellon University, 2009.

[17] W. K. Wilkie, J. E. Warren, M. W. Thompson, et al. The Heliogyro Reloaded. In *JANNAF 5th Spacecraft Propulsion Subcommittee Joint Meeting*, 2011.

[18] W. K. Wilkie, J. E. Warren, L. G. Horta, et al. Heliogyro Solar Sail Research at NASA. In M. Macdonald, editor, *Advances in Solar Sailing*, Springer Praxis Books, pages 631–650. Springer, Berlin, Heidelberg, 2014.

[19] D. Guerrant. *Performance quantification of heliogyro solar sails using structural, attitude, and orbital dynamics and control analysis*. PhD thesis, University of Colorado, 2015.

[20] W. K. Wilkie, J. Warren, L. G. Horta, et al. Recent advances in heliogyro solar sail structural dynamics, stability, and control research. In *2nd AIAA Spacecraft Structures Conference*, page 0431, 2015.

[21] S. Chad Gibbs and E. H. Dowell. Solarelastic stability of the heliogyro. In *Advances in Solar Sailing*, pages 651–665. Springer, 2014.

[22] D. Guerrant and D. Lawrence. Heliogyro solar sail blade twist stability analysis of root and reflectivity controllers. In *AIAA Guidance, Navigation, and Control Conference*, page 4842, 2012.

[23] D. V. Guerrant and D. A. Lawrence. Nonlinear torsional dynamics and control of heliogyro solar sail blades. In *2nd AIAA Spacecraft Structures Conference*, page 0435, 2015.

[24] J. Heiligers, D. Guerrant, and D. Lawrence. Solving the heliogyro's inverse problem. In *AIAA/AAS Astrodynamics Specialist Conference*. American Institute of Aeronautics and Astronautics, 2016.

[25] D. Guerrant and D. Lawrence. Tactics for Heliogyro Solar Sail Attitude Control via Blade Pitching. *Journal of Guidance, Control, and Dynamics*, 38(9):1785–1799, 2015. Publisher: American Institute of Aeronautics and Astronautics.

[26] J. Kang and K.-C. Park. Computational Multibody Dynamics of Heliogyro Solar Sail under Spin-Deployment. In *AIAA Scitech 2020 Forum*, Orlando, FL, 2020. American Institute of Aeronautics and Astronautics.

[27] R. Stevens and I. M. Ross. Preliminary Design of Earth-Mars Cyclers Using Solar Sails. *Journal of Spacecraft and Rockets*, 42(1):132–137, 2005.

[28] G. Mengali and A. A. Quarta. Solar-Sail-Based Stopover Cyclers for Cargo Transportation Missions. *Journal of Spacecraft and Rockets*, 44(4): 822–830, 2007.

[29] M. Vergaaij and J. Heiligers. Time-optimal solar sail heteroclinic-like connections for an Earth-Mars cycler. *Acta Astronautica*, 152:474–485, 2018.

[30] J. Diebel. Representing attitude: Euler angles, unit quaternions, and rotation vectors. *Matrix*, 58, 01 2006.

[31] B. Wie. *Space Vehicle Dynamics and Control*. AIAA education series. American Institute of Aeronautics and Astronautics, 2008.

[32] Y. Tsuda, T. Saiki, R. Funase, and Y. Mimasu. Generalized Attitude Model for Spinning Solar Sail Spacecraft. *Journal of Guidance, Control, and Dynamics*, 36(4):967–974, 2013. Publisher: American Institute of Aeronautics and Astronautics.

[33] E. M. Standish, J. G. Williams, et al. Orbital ephemerides of the sun, moon, and planets. *Explanatory supplement to the astronomical almanac*, pages 279–323, 1992.

[34] F. G. Losada. Controllability of solar-sail orbits in the Earth-Moon system. Master's thesis, TU Delft, 2019.

[35] G. G. Wawrzyniak and K. C. Howell. Numerical techniques for generating and refining solar sail trajectories. *Advances in Space Research*, 48(11): 1848–1857, 2011.

[36] J. T. Betts. Survey of Numerical Methods for Trajectory Optimization. *Journal of Guidance, Control, and Dynamics*, 21(2):193–207, 1998.

[37] J. T. Betts. *Practical Methods for Optimal Control and Estimation Using Nonlinear Programming, Second Edition*. Society for Industrial and Applied Mathematics, second edition, 2010.

[38] M. Kelly. Transcription methods for trajectory optimization: a beginners tutorial. *arXiv: Optimization and Control*, 2017.

[39] E. Pellegrini and R. P. Russell. On the Computation and Accuracy of Trajectory State Transition Matrices. *Journal of Guidance, Control, and Dynamics*, 39(11):2485–2499, November 2016.

[40] O. Montenbruck and E. Gill. *Satellite Orbits*, volume 1. Springer-Verlag Berlin Heidelberg, 2000.

[41] C. Büskens and D. Wassel. The ESA NLP Solver WORHP. In G. Fasano and J. D. Pintér, editors, *Modeling and Optimization in Space Engineering*, pages 85–110. Springer New York, New York, NY, 2013.

[42] F. Biscani and D. Izzo. A parallel global multiobjective framework for optimization: pagmo. *Journal of Open Source Software*, 5(53):2338, 2020.

[43] WORHP. Users' Guide to WORHP 1.14. Technical report, Steinbeis-Forschungszentrum Optimierung, Steuerung und Regelung, 2020.

[44] P. Virtanen, R. Gommers, T. E. Oliphant, et al. SciPy 1.0: Fundamental Algorithms for Scientific Computing in Python. *Nature Methods*, 17:261–272, 2020.